A small molecule cocktail for robust induction of blood-brain barrier properties

Gergő Porkoláb[1,2], Mária Mészáros[1], Anikó Szecskó[1,2], Judit P. Vigh[1,2], Fruzsina R. Walter[1], Ricardo Figueiredo[3], Ildikó Kálomista[4], Gaszton Vizsnyiczai[1], Jeng-Shiung Jan[5], Fabien Gosselet[6], Monika Vastag[4], Szilvia Veszelka[1] & Mária A. Deli[1,✉]

[1]Institute of Biophysics, Biological Research Centre, Eötvös Loránd Research Network, Szeged, Hungary
[2]Doctoral School of Biology, University of Szeged, Szeged, Hungary
[3]GenXPro GmbH, Frankfurt am Main, Germany
[4]In vitro Metabolism Laboratory, Gedeon Richter Plc., Budapest, Hungary
[5]Department of Chemical Engineering, National Cheng Kung University, Tainan, Taiwan
[6]Laboratoire de la Barriére Hémato-Encéphalique (LBHE), Université d'Artois, Lens, France

✉Correspondence: deli.maria@brc.hu

Abstract

Blood-brain barrier (BBB) models derived from human stem cells are powerful tools to improve our understanding of human cerebrovascular diseases and facilitate drug development for the brain. Yet providing endothelial cells with the appropriate molecular cues to both retain a vascular identity and acquire BBB characteristics remains challenging. Here we present cARLA, an easy-to-use and affordable small molecule cocktail that robustly induces BBB properties *in vitro*. By activating cyclic AMP and Wnt/β-catenin signaling while inhibiting the transforming growth factor beta (TGF-β) pathway, cARLA synergistically enhances barrier tightness in a range of BBB models. We demonstrate that, upon cARLA treatment, human stem cell-derived endothelial cells have lower rates of transcytosis, higher glycocalyx density and increased efflux pump activity with a shift in gene expressional profile towards the *in vivo* brain endothelial signature. Our work provides mechanistic insight into how endothelial signaling is orchestrated during BBB maturation and leverages this to advance the prediction of drug delivery to the human brain.

Endothelial cells (ECs) lining the smallest blood vessels in the brain possess unique anatomical and functional properties, collectively known as the BBB[1]. Through specialized tight junction complexes, low rates of vesicular transcytosis, a negatively charged glycocalyx as well as efflux and influx transport systems, the BBB precisely controls the composition of the neural microenvironment[2]. While this protects the brain from harmful substances, the barrier also prevents most drugs from entering the central nervous system, hindering drug development for neurological diseases[3]. Additionally, BBB breakdown is a hallmark of a range of neuropathologies[4,5], yet these processes are incompletely understood in humans at the molecular level. To improve the prediction of drug delivery to the brain and provide mechanistic insight on BBB (dys)function, there is a need for *in vitro* models that faithfully mimic the human BBB and can be used for drug development in human organs-on-chips[6].

Gold standard culture models of the BBB use primary brain microvascular ECs isolated from animal tissue[7]. However, there are major interspecies differences in the BBB proteome related to drug transport[8,9,10], which negatively impacts the translatability of findings from animal models to clinical trials. As a human alternative with good scalability, several BBB models have been established using induced pluripotent stem cells[11,12,13,14,15,16,17,18,19,20,21] or $CD34^+$ hematopoietic stem cells derived from umbilical cord blood[22,23,24,25]. Although the development of these protocols represents a major technological milestone, the resulting models either display a mixed epithelial-endothelial phenotype or have suboptimal barrier properties, which greatly limits their usability[26,27]. To solve this, two-step differentation has emerged as a promising strategy, in which stem cells are first differentiated to ECs and brain-like features are then induced by various techniques including co-culture with other brain cell types[15,22,21].

BBB properties are not intrinsic to ECs, rather, they are promoted and maintained by organ-specific signaling cues *in vivo* from pericytes[28,29,30] and astrocytes[31,32,33]. Picking the right factors that enhance barrier integrity in addition to co-culture signals *in vitro*, however, remains challenging. Treatment with cyclic AMP-elevating agents (pCPT-cAMP, forskolin and the cAMP-specific phosphodiesterase inhibitor Ro-20-1724) has previously been shown to increase resistance across EC monolayers alone, and especially in combination with astrocyte-conditioned medium[34,35,36]. During development, Wnt/β-catenin signaling controls brain angiogenesis[37,38,39] and BBB formation[40,41,42], and this pathway has been activated *in vitro* by Wnt ligands (Wnt-3a, Wnt-7a/b) or small molecules (LiCl, 6-BIO, CHIR99021) to induce a subset of barrier properties[22,43,44,45,46]. Recently, TGF-β receptor antagonists (RepSox, A83-01) have also been demonstrated to elevate junctional tightness in stem cell-derived ECs[47,48] *via* claudin-5, the dominant tight junction protein at the BBB[49].

Since astrocytes can be a source of Wnt ligands[50,51] and Wnt signaling-associated genes were induced by RepSox[47], we hypothesized that these pathways converge during BBB formation, which can be leveraged to increase barrier properties in culture. Here we present cARLA, a small molecule cocktail consisting of pCPT-cAMP+Ro-20-1724+LiCl+A83-01, which robustly induces BBB characteristics in vascular ECs by simultaneously activating cAMP and Wnt/β-catenin signaling while inhibiting the TGF-β pathway.

Results

cARLA synergistically enhances barrier tightness in human stem cell-derived endothelial cells

First, we performed an impedance-based screen of small molecules and recombinant proteins for their ability to enhance barrier integrity in cultured human stem cell-derived ECs supplemented with pericyte-conditioned medium (**Fig. 1a**). This approach allowed us to test selected activators of cAMP and Wnt as well as inhibitors of TGF-β signaling combinatorially (**Fig. 1b**) in a 96-well plate format, in real time. After optimizing treatment durations and concentrations (**Extended Data Fig. 1a-f**), we asked whether combining Wnt activation with TGF-β inhibition increases barrier integrity compared to targeting single pathways. Interestingly, we observed an increase but only by specific combinations, most effectively by LiCl+A83-01 (**Extended Data Fig. 2a-h**).

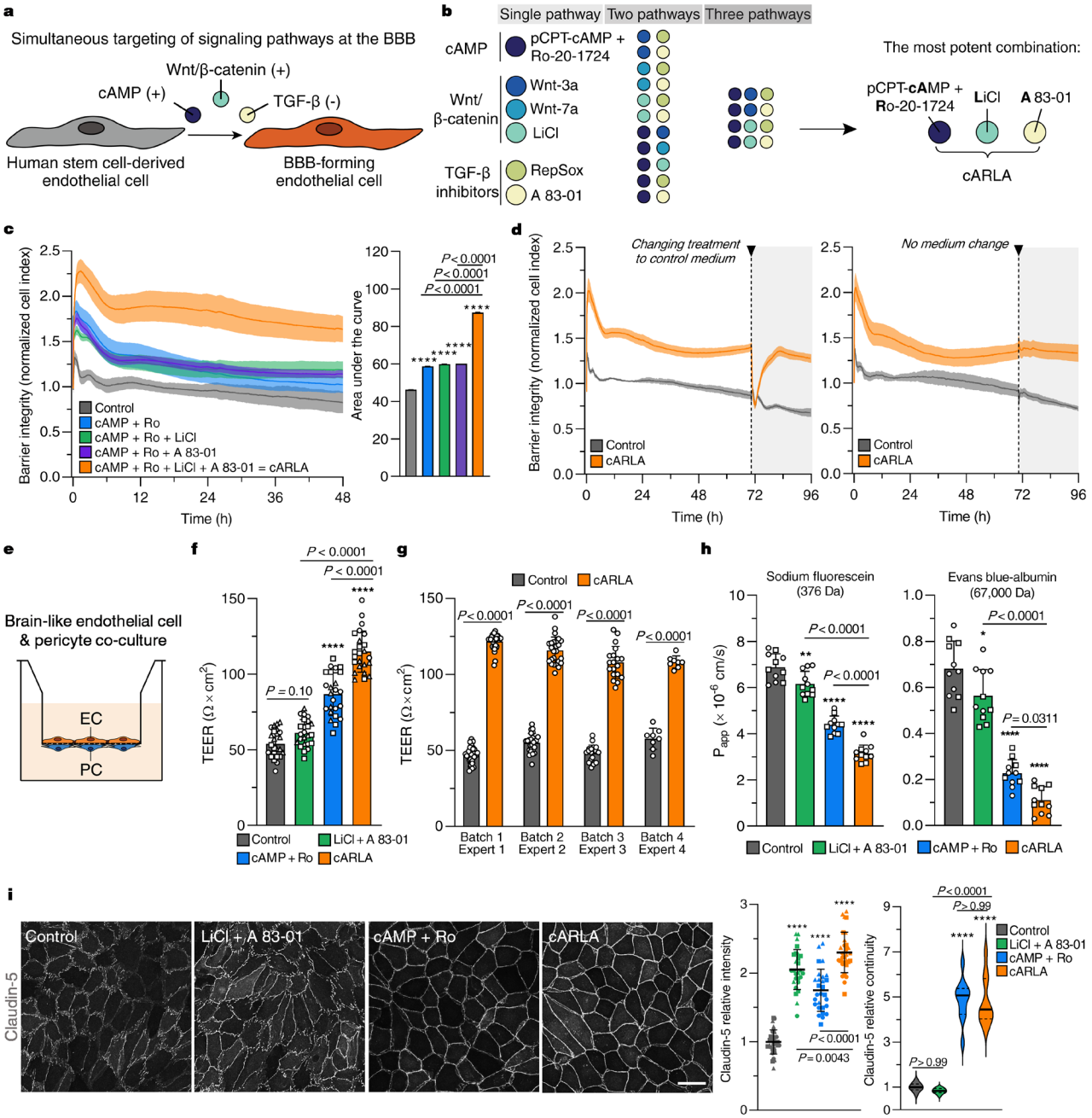

Fig. 1. cARLA synergistically enhances barrier tightness in human stem cell-derived endothelial cells. **a)** Rationale of the study. **b)** Schematic representation of single compounds and their combinations tested in the impedance-based screen. **c)** Barrier integrity of human stem cell-derived EC monolayers supplemented with PC-conditioned medium measured by impedance. Higher normalized cell index values and a higher area under the curve indicates increased barrier integrity. Mean ± SD, ANOVA with Bonferroni's post-hoc test, ****P<0.0001 compared to the control group, n=6. **d)** Impedance kinetics of EC monolayers with or without changing cARLA treatment to control medium at 72 h. Mean ± SD, n=6. **e)** Schematic drawing of the BBB model consisting of human stem cell-derived ECs acquiring brain-like characteristics upon co-culture with PCs. **f)** Transendothelial electrical resistance (TEER) in the co-culture model after 48 h treatment. Mean ± SD, ANOVA with Bonferroni's post-hoc test, ****P<0.0001 compared to the control group, n=24 from 3 independent experiments. **g)** Reproducibility of TEER measurements after 48 h cARLA treatment across experiments, measured by different experts using different batches of cells. Mean ± SD, ANOVA with Bonferroni's post-hoc test, n=82 from 4 independent experiments. **h)** Permeability of sodium fluorescein and Evans blue-albumin across the co-culture model after 48 h treatment. P_{app}: apparent permeability coefficient. Mean ± SD, ANOVA with Bonferroni's post-hoc test, *P<0.05, **P<0.01, ****P<0.0001 compared to the control group, n=11 from 2 independent experiments. **i)** Immunostaining of the tight junction protein claudin-5 in ECs. Bar: 50 µm. Quantification: Mean ± SD for the middle subpanel, median ± quartiles for the right subpanel, ANOVA with Bonferroni's post-hoc test, ****P<0.0001 compared to the control group, n=27-30 from 3 independent experiments.

93 We then asked if Wnt activation by LiCl or TGF-β inhibition by A83-01 can potentiate the barrier
94 integrity-promoting effect of cAMP signaling in ECs. Targeting the cAMP pathway alone by
95 pCPT-cAMP+Ro-20-1724 (cAMP+Ro) resulted in an immediate and potent but diminishing increase
96 in barrier integrity over time (**Fig. 1c**). The addition of either LiCl or A83-01 did not enhance of the
97 effect of cAMP+Ro (**Fig. 1c**). However, the combination of cAMP+Ro+LiCl+A83-01, which we
98 termed as cARLA, greatly and synergistically elevated barrier integrity in ECs (**Fig. 1c**). This effect
99 could be reproduced by other combinations that simultaneously activate cAMP and Wnt as well as
100 inhibit TGF-β signaling (**Extended Data Fig. 3a,b**) but we have found cARLA to be the most potent
101 combination in our screen (**Fig. 1b; Extended Data Fig. 3c**). Furthermore, the effect of cARLA on
102 barrier integrity was long-lasting (>72 h) and resilient to withdrawal of treatment from ECs after 72 h
103 (**Fig. 1d; Extended Data Fig. 4a**).

104 We validated these findings in a BBB model in which human stem cell-derived ECs acquire brain-
105 like characteristics (from now on referred to as brain-like ECs) upon co-culture with pericytes
106 (**Fig. 1e**)[22]. Transendothelial electrical resistance (TEER) was synergistically increased upon cARLA
107 treatment by 2.1-fold compared to the control group (**Fig. 1f; Extended Data Fig. 4b**), an effect
108 highly reproducible across experiments (**Fig. 1g**). Moreover, we measured a lower permeability for
109 tracers sodium fluorescein (2.2-fold) and Evans blue-albumin (7.4-fold compared to the control
110 group) across the co-culture model (**Fig. 1h**), indicating that cARLA tightened both the para- and
111 transcellular BBB. Finally, as a proposed mediator of its barrier tightening effect, cARLA specifically
112 (**Extended Data Fig. 4c)** elevated both staining intensity (2.3-fold) and continuity (4.5-fold) of the
113 tight junction protein claudin-5 at cell borders (**Fig. 1i**).

114 **cARLA promotes barrier maturation and brain endothelial identity revealed by MACE-seq**

115 To investigate gene expressional changes in brain-like ECs upon cARLA treatment, we performed
116 Massive Analysis of cDNA Ends (MACE-seq, **Fig. 2a**).

117 Principal component analysis revealed a sharp separation of control and cARLA samples along
118 principal component 1 (PC1), with low heterogeneity of replicates within each group (**Fig. 2b**).
119 Among the 1,054 upregulated and 1,073 downregulated genes upon cARLA treatment (**Fig. 2c**), we
120 observed key transcripts related to different aspects of BBB function (**Fig. 2d**). For example, *ABCB1*
121 (encoding the efflux pump P-glycoprotein), *ST6GALNAC3* (an enzyme involved in the synthesis of
122 glycocalyx), *SLC2A1* (the glucose transporter GLUT1) and expectedly, *CLDN5* (claudin-5) were
123 upregulated by cARLA. On the other hand, *CAV1* (caveolin-1) as well as *VCAM1*, *MMP2* and *CCL2*
124 (vascular cell adhesion molecule-1, matrix metalloproteinase-2 and the C-C motif ligand-2
125 chemokine, respectively, all involved in pathological BBB disruption) were downregulated (**Fig. 2d**).

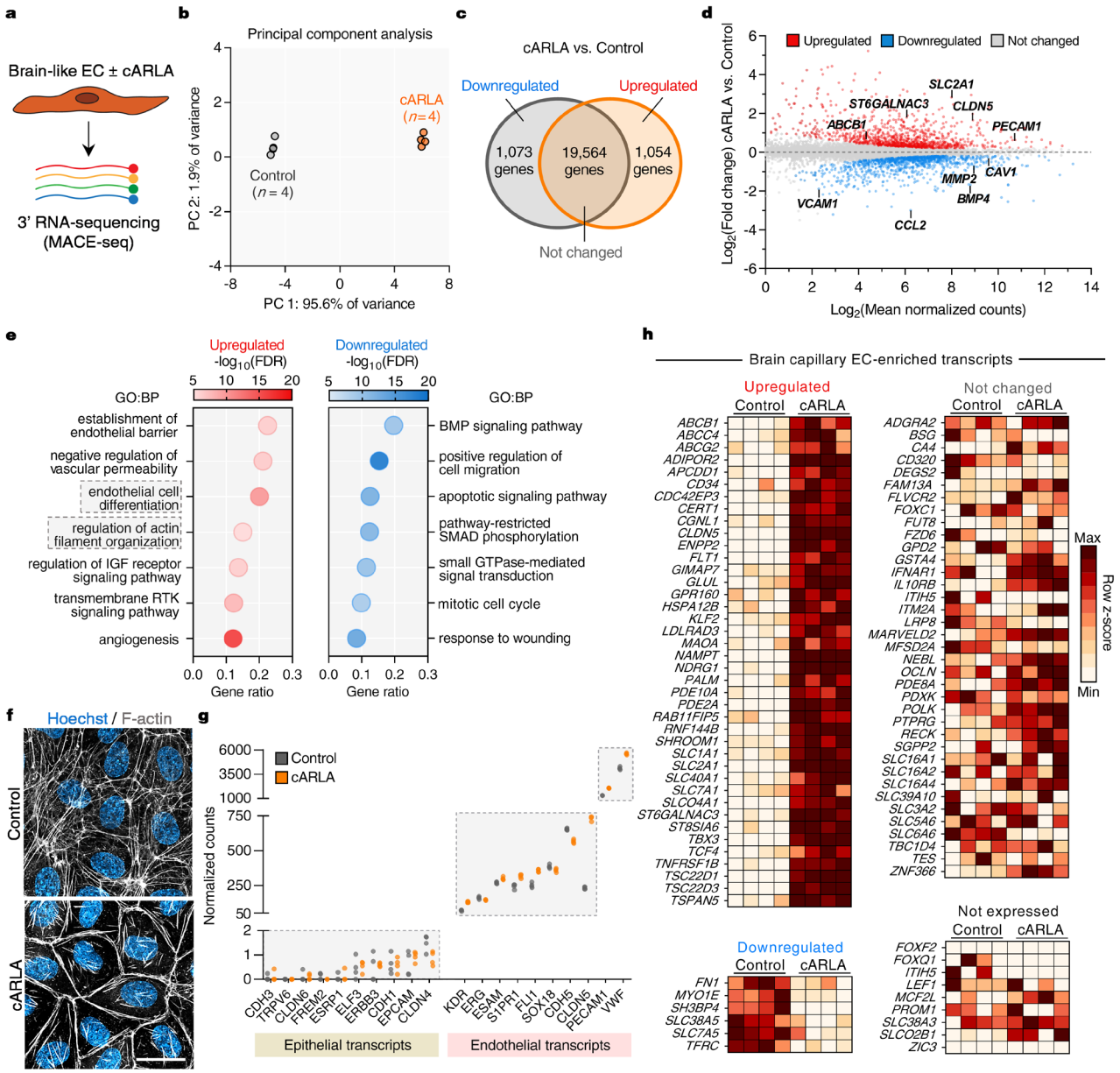

Fig. 2. cARLA promotes barrier maturation and brain endothelial identity revealed by MACE-seq.

a) Schematic drawing of the experimental setup. MACE-seq was performed on samples from brain-like ECs (in co-culture with PCs), with or without 48 h cARLA treatment. **b)** Principal component analysis (PCA) plot of control and cARLA samples. **c)** Venn-diagram showing the number of genes upregulated ($\log_2FC \geq 0.2$ and FDR < 0.01), downregulated ($\log_2FC \geq -0.2$ and FDR < 0.01) or not changed ($|\log_2FC| < 0.2$ and/or FDR ≥ 0.01) upon cARLA treatment. Log_2FC: $\log_2$(fold change), FDR: false discovery rate. **d)** Mean-difference (MD) plot presenting the range and distribution of all transcripts (circles) regarding their mean expression and $\log_2FC$ upon cARLA treatment. Key transcripts related to different aspects of BBB function are highlighted. **e)** Functional enrichment analysis of up- and downregulated gene sets upon cARLA treatment using g:Profiler. Gene Ontology Biological Process (GO:BP) terms are ranked based on their gene ratio (the fraction of differentially expressed genes in a given term) and are colored based on statistical significance (FDR). **f)** Representative staining of F-actin (grey), with or without cARLA treatment. Nuclei were stained with Hoechst (blue). Bar: 40 µm. **g)** Validation of the definitive endothelial nature of human stem cell-derived brain-like ECs. Normalized counts of key epithelial and endothelial transcripts from our dataset are plotted on a 3-segment y-axis covering multiple orders of magnitude. **h)** Scaled heatmap of 92 transcripts that are enriched in mouse brain ECs and are well expressed at the human BBB. Genes upregulated, downregulated or not changed upon cARLA treatment as well as genes not expressed (normalized counts ≤ 1) in this model are shown separately, in alphabetical order. Color coding represents row z-scores after Min-Max normalization, the darkest color corresponding to the highest expression in a given row.

145 On a pathway level, we observed an overrepresentation of genes related to EC differentiation and
146 barrier formation as well as maturation and quiescence (**Fig. 2e**). This was also accompanied by a
147 marked redistribution of F-actin from stress fibers to the cortical actin cytoskeleton (**Fig. 2f**),
148 supporting the maturation of cell-cell contacts.

149 The expression of key endothelial genes in brain-like ECs was orders of magnitude higher than
150 that of epithelial-associated genes, confirming the definitive endothelial nature of the model (**Fig. 2g**).
151 To investigate if cARLA further shifts the gene expression of ECs towards a brain endothelial
152 signature, we examined a set of 92 transcripts that are enriched in brain *vs*. peripheral ECs in mice[50,52]
153 and are well expressed in human brain capillary ECs[53,54]. From this list of not necessarily canonical
154 but BBB-specific genes, 40 were upregulated upon cARLA treatment (**Fig. 2h**), indicating an
155 incomplete yet substantial shift towards the *in vivo* brain capillary EC identity.

156 **cARLA induces a complex BBB phenotype at the mRNA, protein and functional level**

157 MACE-seq profiling revealed that cARLA can influence several aspects of BBB maturation, not
158 just junctional tightness (**Fig. 2d,h; Extended Data Fig. 5a-i**). To explore the ability of cARLA
159 to induce a complex BBB phenotype, we validated findings at the protein and functional level for
160 three selected BBB properties in brain-like ECs (**Fig. 3a**).

161 First, the expression of key enzymes participating in the synthesis of the negatively charged
162 EC glycocalyx was upregulated by cARLA (**Fig. 3b**). This was mirrored by a higher intensity of
163 wheat germ agglutinin (WGA) lectin staining, which specifically recognizes negatively charged sialic
164 acid residues in the glycocalyx, upon cARLA treatment (**Fig. 3c**). Accordingly, we measured a more
165 negative surface charge (Δ -1.5 mV) in ECs treated with cARLA (**Fig. 3d**).

166 Secondly, genes associated with endocytic vesicle formation and nonspecific albumin uptake,
167 downregulated pathways at the BBB, were also decreased by cARLA (**Fig. 3e**). The expression of
168 *PLVAP* (encoding plasmalemmal vesicle-associated protein, a marker of peripheral ECs with high
169 levels of endocytosis) was already low in our model and was not changed by cARLA (**Fig. 3e**).
170 On average, we observed 20-30% lower levels of albumin internalization in ECs upon cARLA
171 treatment (**Fig. 3f)**, with albumin colocalizing with caveolin-1 (**Fig. 3g**). In agreement with this,
172 albumin internalization was sensitive to methyl-β-cyclodextrin inhibiting lipid raft/caveolin-mediated
173 endocytosis, but to a lesser extent in cARLA-treated cells (**Fig. 3h**).

174 Finally, the expression of BBB efflux transporters, such as P-glycoprotein (*ABCB1*), breast cancer-
175 related protein (BCRP, *ABCG2*) and multidrug resistance-related protein 4 (MRP4, *ABCC4*),
176 was upregulated by cARLA (**Fig. 3i**). Staining intensity of P-glycoprotein was also 20% higher in
177 ECs treated with cARLA (**Fig. 3j**). As a functional test of efflux pump activity, we measured the
178 permeability of rhodamine 123, a ligand of efflux pumps, across the co-culture model in blood-
179 to-brain (A-B) and brain-to-blood (B-A) directions (**Fig. 3k**). The efflux ratio of rhodamine 123 was
180 2.1 upon cARLA treatment (a 1.6-fold increase compared to the control group), which could be
181 reduced to 0.98 using verapamil, an efflux pump inhibitor (**Fig. 3l**). These data together indicate

higher glycocalyx density, decreased endocytosis as well as higher activity and appropriate polarity of efflux pumps in brain-like ECs treated with cARLA.

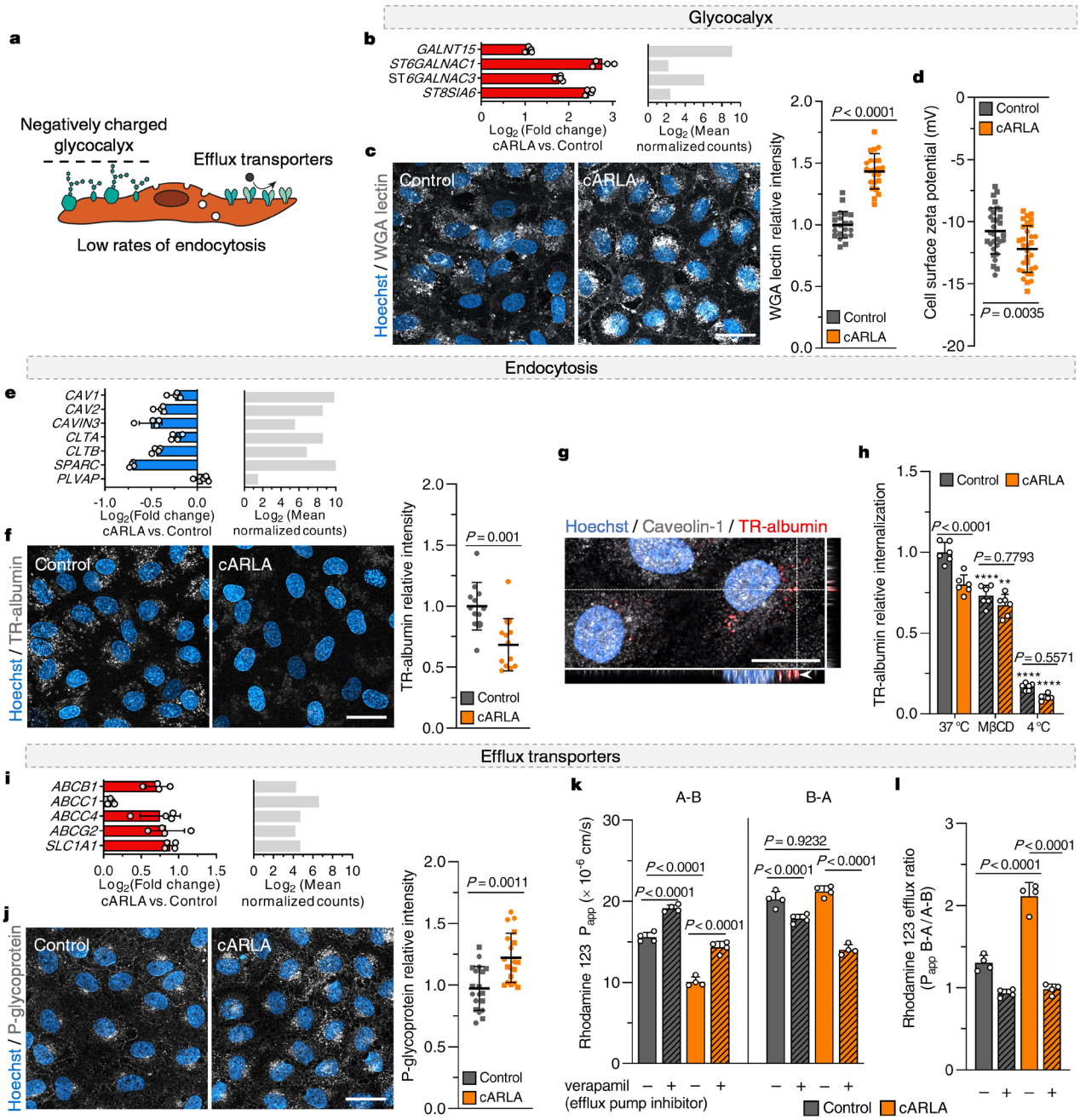

Fig. 3. cARLA induces a complex BBB phenotype with higher glycocalyx density, decreased endocytosis and increased efflux pump activity. a) Schematic drawing of three non-junctional aspects of BBB function induced by cARLA. **b)** Changes in gene expression for key glycocalyx synthesis enzymes at the BBB. Mean ± SD. Red color indicates upregulation upon cARLA treatment. **c)** Wheat germ agglutinin (WGA) lectin staining (grey) labeling negatively charged sialic acid residues in the EC glycocalyx. Nuclei were stained with Hoechst (blue). Bar: 50 µm. Quantification (right panel): Mean ± SD, unpaired t-test, t=11.43, df=43, n=22-24 from 2 independent experiments. **d)** Cell surface zeta potential measurement in ECs. Mean ± SD, unpaired t-test, t=3.045, df=60, n=31 from 2 independent experiments. **e)** Changes in gene expression for mediators of endocytic vesicle formation and nonspecific albumin uptake in ECs. Mean ± SD. Blue color indicates downregulation upon cARLA treatment. **f)** Texas Red (TR)-labeled albumin (grey) internalization in ECs visualized by live cell confocal microscopy. Nuclei were stained with Hoechst (blue). Bar: 50 µm. Quantification (right panel): Mean ± SD, unpaired t-test, t=3.786, df=22, n=12. **g)** Representative immunostaining of caveolin-1 (grey) after TR-albumin (red) internalization in control ECs. YZ (right) and XZ (down) projections of Z-stacks are shown at the level of crosshairs. The arrowhead points to caveolin-1$^+$ TR-albumin$^+$ structures. Nuclei were stained with Hoechst (blue). Bar: 30 µm. **h)** TR-albumin internalization in ECs quantified by fluorescent spectrophotometry. MβCD: randomly methylated β-cyclodextrin.

Incubation at 4 °C inhibits energy-dependent uptake processes. Mean ± SD, two-way ANOVA with Bonferroni's post-hoc test, $^{**}P<0.01$, $^{****}P<0.0001$ compared to its respective 37 °C group, $n=6$. **i)** Changes in gene expression for key efflux transporters at the BBB. Mean ± SD. Red color indicates upregulation upon cARLA treatment. **j)** P-glycoprotein (P-gp, encoded by *ABCB1*) immunostaining (grey) in ECs. Nuclei were stained with Hoechst (blue). Bar: 50 µm. Quantification (right panel): Mean ± SD, unpaired t-test, $t=4.065$, $df=36$, $n=19$ from 2 independent experiments. **k)** Bidirectional permeability of rhodamine 123, a ligand of efflux pumps, across the BBB co-culture model. P_{app}: apparent permeability coefficient. Mean ± SD, two-way ANOVA with Bonferroni's post-hoc test, $n=4$. **l)** Efflux ratio of rhodamine 123 calculated from the same experiment. Mean ± SD, two-way ANOVA with Bonferroni's post-hoc test, $n=4$.

Targeted pathways converge on Wnt/β-catenin signaling to mediate the effect of cARLA

We then asked how the synergistic effect of cARLA on barrier tightness is orchestrated in brain-like ECs. The STRING database proposed a network of interactions between effector transcription factors of cAMP, Wnt and TGF-β pathways, with β-catenin taking center stage (**Fig. 4a**).

Indeed, we observed a robust induction of Wnt/β-catenin signaling-associated genes at the mRNA level (**Fig. 4b**). Furthermore, both staining intensity and nuclear/non-nuclear ratio of β-catenin were synergistically elevated by cARLA (**Fig. 4c**), indicating a convergence of targeted pathways on Wnt signaling. Active β-catenin was visibly present in the nucleus upon cARLA treatment without disruption of junctional β-catenin or VE-cadherin (**Fig. 4c, Extended Data Fig. 6a**), in concordance with the upregulation of *RAPGEF5*, a mediator of β-catenin nuclear import (**Fig. 4b**).

To investigate how a highly active state of Wnt/β-catenin signaling contributes to the effect of cARLA, we pharmacologically blocked this pathway at two different points **(Fig. 4d**). ICG-001 specifically inhibits the β-catenin-CREB-binding protein (CBP) interaction in the nucleus, while XAV 939 blocks the pathway upstream of nuclear translocation (**Fig. 4d**). We titrated these inhibitors so that they do not interfere with basal barrier integrity (**Extended Data Fig. 6b,c**) but block the effect of elevated levels of Wnt signaling (**Fig. 4e,f**). ICG-001 moderately, whereas XAV 939 more potently reduced the effect of cARLA, almost to the level of cAMP+Ro treatment (**Fig. 4e,f**). Similar effects were observed measuring TEER (**Fig. 4g**) and fluorescein permeability (**Fig. 4h**) across the co-culture model. These data indicate that highly active Wnt/β-catenin signaling is necessary for the effect of cARLA on barrier integrity, with the β-catenin-CBP interaction being involved in the establishment of junctional tightness.

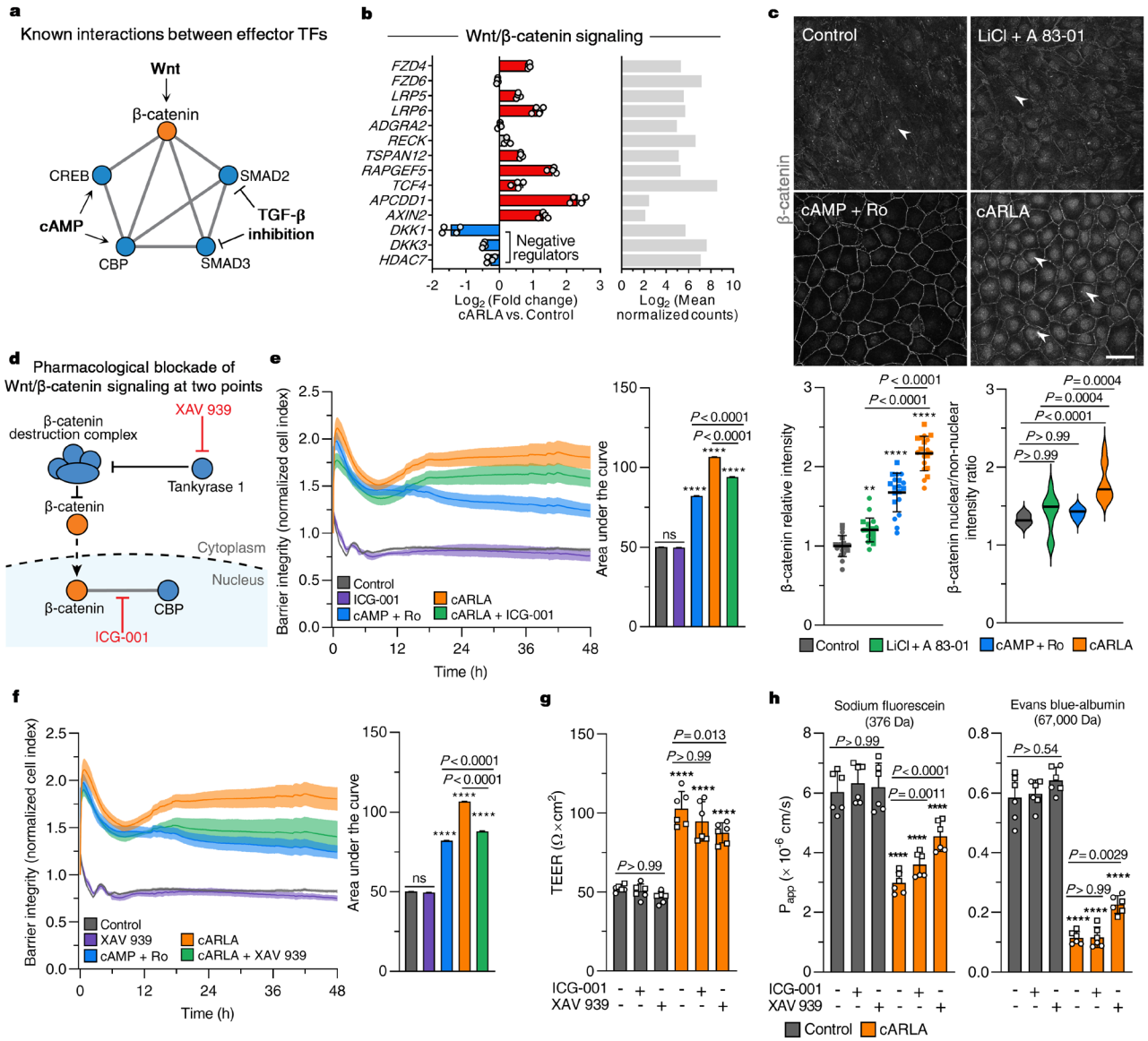

Fig. 4. Targeted pathways converge on Wnt/β-catenin signaling to mediate the effect of cARLA. **a)** Schematic drawing of known interactions between effector transcription factors (TFs) of cAMP, Wnt and TGF-β signaling. **b)** Changes in gene expression related to Wnt/β-catenin signaling. Mean ± SD. Red and blue color indicates up- and downregulation, respectively, upon cARLA treatment. **c)** Immunostaining of β-catenin in ECs. Arrowheads point to nuclear β-catenin, a hallmark of active Wnt signaling. Bar: 50 µm. Quantification: Mean ± SD for the lower left subpanel, median ± quartiles for the lower right subpanel, ANOVA with Bonferroni's post-hoc test, **P<0.01, ****P<0.0001 compared to the control group, n=20 from 2 independent experiments. **d)** Schematic drawing of the mechanism of action for ICG-001 and XAV 939, inhibitors of Wnt signaling at different levels of the pathway. Barrier integrity measured by impedance in EC monolayers, with or without **e)** ICG-001 (5 µM) and **f)** XAV 939 (1 µM). Higher normalized cell index values and a higher area under the curve indicates increased barrier integrity. Mean ± SD, ANOVA with Bonferroni's post-hoc test, ****P<0.0001 compared to the control group, n=5-6. **g)** Measurement of TEER and **h)** permeability for sodium fluorescein and Evans blue-albumin across the co-culture, with or without ICG-001 and XAV 939. P_{app}: apparent permeability coefficient. Mean ± SD, ANOVA with Bonferroni's post-hoc test. ****P<0.0001 compared to its respective treatment in the control group, n=6 from 2 independent experiments.

246 **cARLA improves the prediction of drug- and nanoparticle delivery across the human BBB**

247 To put cARLA into practice, we first assessed the penetration of ten clinically used small molecule
248 drugs (**Supplementary Table 1,2**) across the co-culture model, with or without cARLA treatment.
249 Drugs were selected to include different routes of penetration across the BBB, such as passive
250 diffusion as well as efflux and influx transport. In blood-to-brain (A-B) direction, we measured a
251 lower permeability for efflux pump ligands vinblastine, loperamide, salicylic acid and verapamil upon
252 cARLA treatment (**Fig. 5a**). Conversely, cARLA increased the permeability of tacrine (influx) and
253 propranolol (passive lipophilic, influx) across the co-culture model. As a result, the cARLA-treated
254 human BBB model could correctly discriminate between drugs that readily enter the central nervous
255 system and those that do not (**Fig. 5a**). Treatment with cARLA also elevated the efflux ratio of
256 loperamide and methotrexate (with a trend for vinblastine and verapamil), indicating improved
257 vectorial transport across the BBB model (**Fig. 5b**).

258 Similar tendencies were seen regarding the extent of drug penetration across the BBB model
259 (**Fig. 5c**) given as *in vitro* unbound brain-to-plasma partition coefficients ($K_{p,uu,brain}$)[22,25,55].
260 Importantly, cARLA increased the level of correlation between human *in vitro* $K_{p,uu,brain}$ values and
261 *in vivo* brain penetration data from rats[55] and non-human primates[56] (**Fig. 5d**). In the case of
262 verapamil, the only drug on our list with human clinical $K_{p,uu,brain}$ data available, the cARLA-treated
263 BBB model well approximated the human *in vivo* value (**Fig. 5e**) and was second only to non-human
264 primate *in vivo* data among predictive models[22,25,56].

265 To test the effect of cARLA on the penetration of nanocarriers across the co-culture model, we
266 assessed the permeability of polypeptide nanoparticles (NPs) with or without the BBB-specific
267 targeting ligand glutathione (GSH; **Fig. 5f**). We measured a 20% lower permeability for non-targeted
268 NPs across the cARLA-treated model compared to the control group (**Fig. 5g**). Notably,
269 GSH-targeted NPs had a higher permeability compared to non-targeted NPs across the cARLA-
270 treated but not the control model (**Fig. 5g**), which was also mirrored by their internalization in ECs
271 (**Fig. 5h**). Taken together, these results indicate that cARLA can potentially be used to improve the
272 *in vitro* prediction of therapeutic drug- and NP delivery across the human BBB.

273

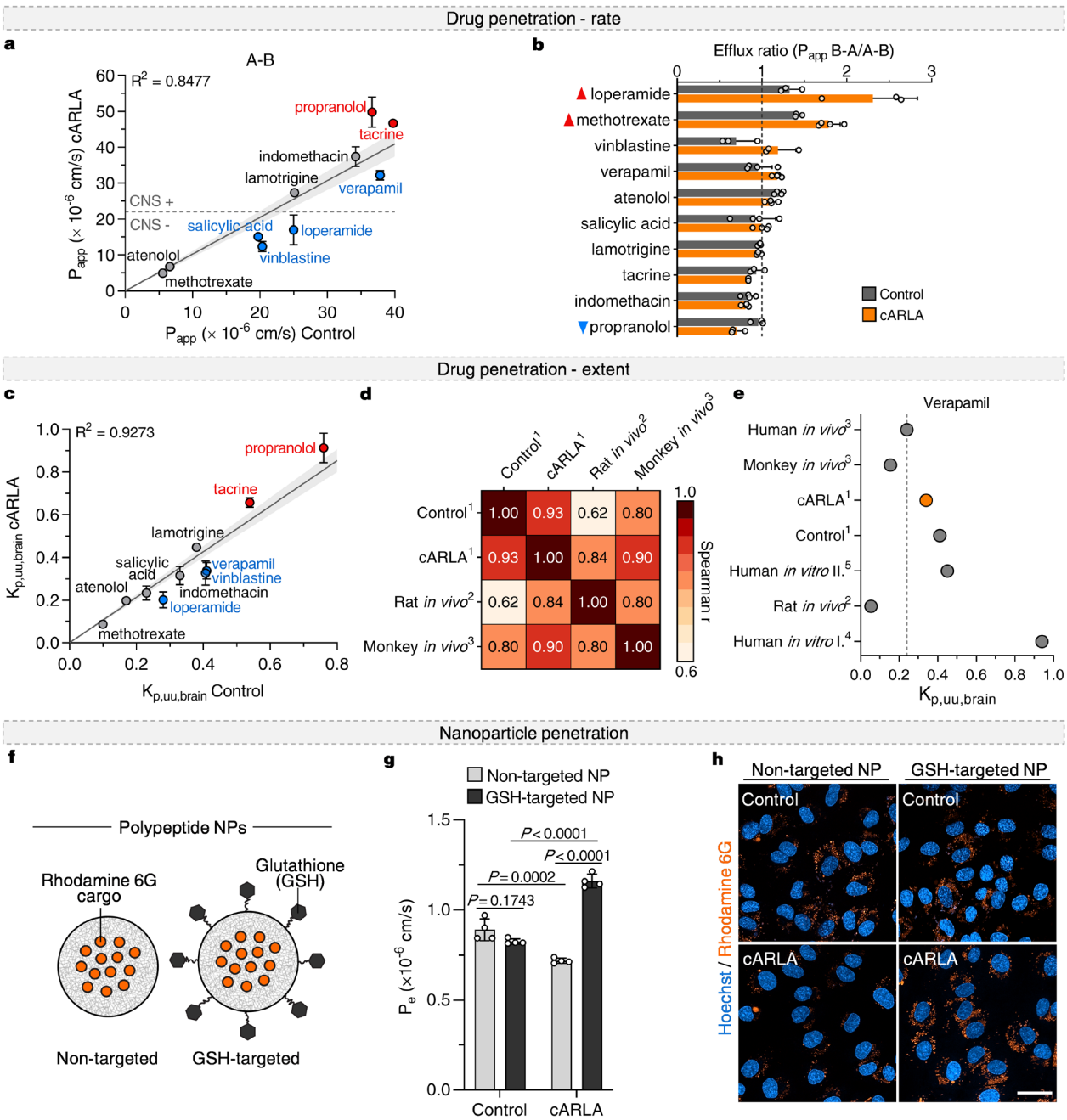

Fig. 5. cARLA improves the *in vitro* prediction of drug- and nanoparticle delivery across the human BBB. a) Permeability of 10 clinically used small molecule drugs in blood-to-brain (A-B) direction across the BBB co-culture model, with or without cARLA treatment. P_{app}: apparent permeability coefficient, CNS: central nervous system. Red and blue color indicates higher and lower permeability, respectively, for a given drug upon cARLA treatment ($P < 0.05$). Mean ± SD for symbols, n=3-4. Line of best fit with 95% convidence intervals and R^2 value from a simple linear regression are shown. **b)** Drug efflux ratios in the co-culture model. Mean ± SD, multiple unpaired t-tests with Welch's correction, n=3-4. Upward red and downward blue triangles indicate higher and lower efflux ratios, respectively. **c)** *In vitro* unbound brain-to-plasma partition coefficient ($K_{p,uu,brain}$) of drugs across the co-culture model, with or without cARLA treatment. Red and blue color indicates higher and lower values, respectively, for a given drug upon cARLA treatment ($P < 0.05$). Mean ± SD for symbols, n=3-4. Line of best fit with 95% convidence intervals and R^2 value from a simple linear regression are shown, respectively, upon cARLA treatment ($P < 0.05$). **d)** Correlation heatmap of *in vitro* $K_{p,uu,brain}$ values for the whole set of drugs from our model with *in vivo* $K_{p,uu,brain}$ data from rats and non-human primates. Numbers inside boxes are Spearman's correlation coefficients. Data obtained from: [1]present study, [2]Fridén *et al.*, 2009 (ref 55) and [3]Sato *et al.*, 2021 (ref 56). **e)**

289 Comparison of $K_{p,uu,brain}$ measured *in vivo* in humans with its predictive models for verapamil. Points are means,
290 data obtained from articles above as well as from [4]Cecchelli *et al*., 2014 (ref 22), and [5]Moya *et al*., 2021 (ref 25). **f)**
291 Schematic drawing of non-targeted and GSH-targeted polypeptide nanoparticles (NPs) carrying rhodamine 6G
292 cargo. **g)** Permeability of non-targeted and GSH-targeted NPs across the co-culture BBB model measured by
293 fluorescent spectrophotometry. Mean ± SD, two-way ANOVA with Bonferroni's post-hoc test, *n*=4. **h)**
294 Representative live cell confocal microscopy images showing the internalization of non-targeted and GSH-targeted
295 NPs carrying rhodamine 6G (orange) in ECs, with or without cARLA treatment. Nuclei were stained with Hoechst
296 (blue). Bar: 50 µm.

297 **The effect of cARLA on barrier tightness is reproducible in additional BBB culture models**

298 Finally, we asked if cARLA could improve barrier properties in other *in vitro* BBB models widely
299 used for complementing results from animal studies. For this reason, we selected two models of
300 rodent origin, namely the mouse brain EC line bEnd.3 in monoculture and a rat primary brain EC-
301 pericyte-astrocyte co-culture model[57] (**Fig. 6a**). Barrier integrity measured by impedance was greatly
302 elevated by cARLA in both models, albeit to a different extent and with different kinetics (**Fig. 6b,c**).
303 Of note, the optimal treatment concentration of cARLA and its components were also different
304 between mouse bEnd.3 cells (**Extended Data Fig. 7a-f**), primary rat brain ECs (**Extended Data**
305 **Fig. 8a-f**) and human brain-like ECs, emphasizing a need for optimization in each model.

306 As validation, we measured a 2.1-fold increase in TEER (**Fig. 6d**) and decreased permeability of
307 sodium fluorescein (1.6-fold) and Evans blue-albumin (3.4-fold) tracers across bEnd.3 monolayers
308 upon cARLA treatment (**Fig. 6e**). In the primary rat co-culture model, a 2.9-fold increase in TEER
309 (**Fig. 6f**) as well as a 2.1-fold and 1.93-fold decrease in permeability was seen for sodium fluorescein
310 and Evans blue-albumin, respectively (**Fig. 6g**). Similarly to human brain-like ECs, treatment with
311 cARLA synergistically and specifically elevated the staining intensity of endothelial claudin-5 in
312 mouse bEnd.3 cells (**Fig. 6h, Extended Data Fig. 7g**) and in the rat primary co-culture model (**Fig. 6i,**
313 **Extended Data Fig. 8g**). These data suggest a conserved effect of cARLA between BBB models of
314 different origin and complexity, further broadening the usability of this small molecule cocktail.

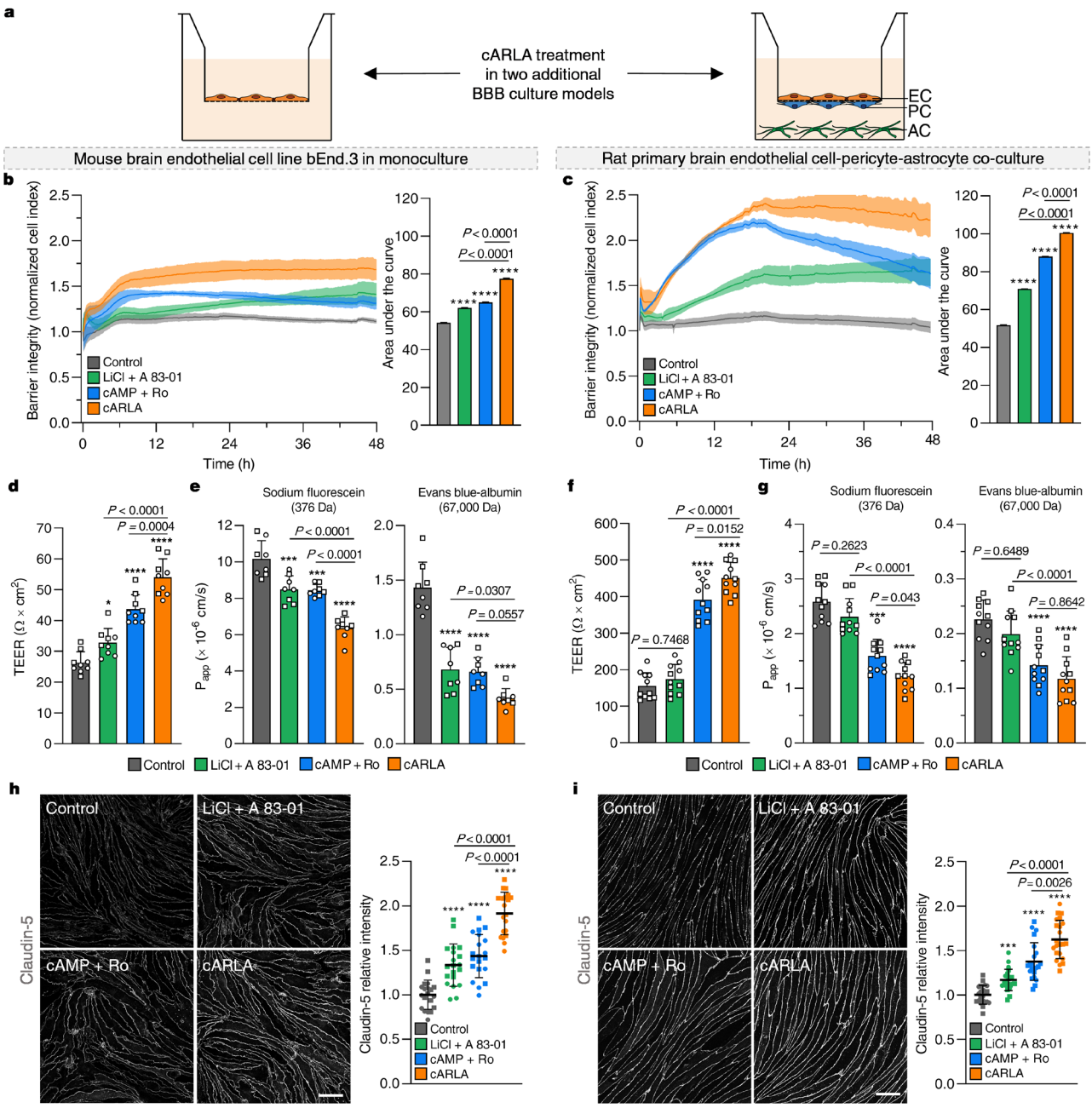

Fig. 6. The effect of cARLA on barrier tightness is reproducible in two additional BBB culture models. **a)** Schematic drawing of two widely used BBB culture models with different complexity in which cARLA treatment was additionally tested. Real-time measurement of barrier integrity by impedance **b)** in mouse bEnd.3 cells and **c)** in rat primary brain capillary ECs. Higher normalized cell index values and a higher area under the curve indicates increased barrier integrity. Mean ± SD, ANOVA with Bonferroni's post-hoc test, ****P<0.0001 compared to the control group, n=5-6 for both panels. **d)** Measurement of TEER and **e)** permeability for sodium fluorescein and Evans blue-albumin across mouse bEnd.3 monolayers after 48h treatment. P_{app}: apparent permeability coefficient. Mean ± SD, ANOVA with Bonferroni's post-hoc test, *P<0.05, ***P<0.001, ****P<0.0001 compared to the control group, n=8 from 2 independent experiments for both panels. Similarly, **f)** TEER and **g)** tracer permeability was measured in the rat primary cell-based co-culture BBB model. Mean ± SD, ANOVA with Bonferroni's post-hoc test, ***P<0.001, ****P<0.0001 compared to the control group, n=11 from 2 independent experiments for both panels. Immunostaining of the tight junction protein claudin-5. **h)** in mouse bEnd.3 cells and **i)** in rat primary brain capillary ECs from the co-culture. Bar: 50 µm. Quantification (right subpanels): Mean ± SD, ANOVA with Bonferroni's post-hoc test, ****P<0.0001 compared to the control group, n=20-22 from 2 independent experiments for both panels.

Discussion

In the past decade, several laboratories established BBB models derived from human stem cells[11,12,13,14,15,16,17,18,19,20,21,22,23,24,25]. This technology can revolutionize drug development for the brain and improve our understanding of human BBB function in health and disease. Yet there is consensus in the field that existing differentiation protocols need serious improvement to faithfully recapitulate both the endothelial identity and complexity of the human BBB[26,58,59,60]. Motivated by the unmet need for an approach that is easily adaptable, efficient and reproducible, here we developed cARLA, a small molecule cocktail that robustly induces BBB characteristics in vascular ECs.

There are multiple ways to improve BBB properties *in vitro*. Co-culture with astrocytes and/or pericytes have long been described to enchance BBB integrity in primary brain ECs[57,61]. This technique was also adapted to human stem cell-based models[11,12,13,14,15,16,18,19,21,24], including the one we used in this study[22]. However, even if co-culture signals are present, stem cell-derived definitive endothelial models have weak junctional tightness[15,21,22]. Thus, additional factors are needed to facilitate BBB maturation. Overexpression of a combination of general- and brain EC-specific transcription factors using adenoviral vectors has recently been shown to increase barrier integrity in stem cell-derived ECs[62] by approximately 40%. Additionally, overexpression of three general EC transcription factors trans-differentiated cells with a mixed epithelial-endothelial identity to vascular ECs that display a subset of BBB properties[27]. Although transcriptional reprogramming holds promise, it is technically challenging and relatively expensive, making it difficult to be adapted by other laboratories. Similarly, selective passaging has been demonstrated to improve the correct localization of junctional proteins and decrease the permeability of fluorescein across EC monolayers[21]. However, this method is highly time- and labor-intensive compared to other approaches. Small molecule factors, on the other hand, are easy-to-use, affordable and can rapidly induce BBB properties, if chosen appropriately.

Soluble activators of cAMP[34,35,36], Wnt/β-catenin[22,43,44,45,46] and retinoic acid[12] signaling as well as inhibitors of the TGF-β[47,48] pathway have separately been shown to elevate different aspects of BBB function *in vitro*. In contrast to targeting single pathways, Praça *et al*. used Wnt-3a, VEGF and retinoic acid to simultaneously activate multiple pathways during EC differentiation[15]. These pathways, however, did not effectively potentiate each others' effect on barrier tightness[16]. The strength of our approach compared to previous studies is that we performed a high-throughput, combinatorial screen of soluble factors for their ability to increase barrier tightness in ECs. This allowed us to discover a novel interaction between cAMP, Wnt/β-catenin and TGF-β signaling at the BBB *in vitro* and thus, rationally develop a small molecule cocktail with optimal composition. We demonstrated that cARLA synergistically elevates barrier tightness in ECs *via* claudin-5 and shown that mechanistically, this effect is mediated by targeted pathways converging on Wnt/β-catenin signaling. Another strength of our study over previous work is that cARLA induces several aspects of BBB function, which we validated at the mRNA, protein and functional levels. Added to that, we directly put cARLA into practice and showed that it can potentially improve the *in vitro* prediction of drug- and NP delivery across the human BBB.

Importantly, the aim of our study was not to establish a new BBB model but to develop an approach that can be applied to a range of models. To this end, we put emphasis on reproducibility using additional BBB models, namely the mouse brain EC line bEnd.3 and a primary rat brain EC-pericyte-astrocyte co-culture model[57]. Although it is a limitation of our study that the interactions mediating the effect of cARLA were not yet proven *in vivo*, the fact that its synergistic effect is reproducible across BBB models of different species and complexity is promising. Whether the efficacy of cARLA can be further improved by other cues such as fluid flow and organ-on-a-chip technology[6,19,63], 3D microenvironment[64] or basement membrane composition[65] remains to be explored.

Since its ease of use, high efficacy and reproducibility, cARLA has the potential to be used in a variety of BBB culture models across laboratories to advance drug development for the human brain. We envision that our study will also boost future research in understanding interactions between signaling pathways that govern the formation, maturation and maintenance of the BBB.

References

1. Zlokovic, B.V. The Blood-Brain Barrier in Health and Chronic Neurodegenerative Disorders. *Neuron* **57**, 178-201 (2008).
2. Abbott, N.J., Patabendige, A.A., Dolman, D.E., Yusof, S.R. & Begley, D.J. Structure and function of the blood-brain barrier. *Neurobiol Dis* **37**, 13-25 (2010).
3. Pardridge, W.M. Drug transport across the blood-brain barrier. *J Cereb Blood Flow Metab* **32**, 1959-1972 (2012).
4. Munji, R.N. et al. Profiling the mouse brain endothelial transcriptome in health and disease models reveals a core blood-brain barrier dysfunction module. *Nat Neurosci* **22**, 1892-1902 (2019).
5. Sweeney, M.D., Zhao, Z., Montagne, A., Nelson, A.R. & Zlokovic, B.V. Blood-Brain Barrier: From Physiology to Disease and Back. *Physiol Rev* **99**, 21-78 (2019).
6. Ingber, D.E. Human organs-on-chips for disease modelling, drug development and personalized medicine. *Nature Reviews Genetics* **23**, 467-491 (2022).
7. Helms, H.C. et al. In vitro models of the blood-brain barrier: An overview of commonly used brain endothelial cell culture models and guidelines for their use. *J Cereb Blood Flow Metab* **36**, 862-890 (2016).
8. Uchida, Y. et al. Quantitative targeted absolute proteomics of human blood-brain barrier transporters and receptors. *J Neurochem* **117**, 333-345 (2011).
9. Shawahna, R. et al. Transcriptomic and quantitative proteomic analysis of transporters and drug metabolizing enzymes in freshly isolated human brain microvessels. *Mol Pharm* **8**, 1332-1341 (2011).
10. Uchida, Y. et al. Comparison of Absolute Protein Abundances of Transporters and Receptors among Blood-Brain Barriers at Different Cerebral Regions and the Blood-Spinal Cord Barrier in Humans and Rats. *Mol Pharm* **17**, 2006-2020 (2020).
11. Lippmann, E.S. et al. Derivation of blood-brain barrier endothelial cells from human pluripotent stem cells. *Nat Biotechnol* **30**, 783-791 (2012).
12. Lippmann, E.S., Al-Ahmad, A., Azarin, S.M., Palecek, S.P. & Shusta, E.V. A retinoic acid-enhanced, multicellular human blood-brain barrier model derived from stem cell sources. *Sci Rep* **4**, 4160 (2014).
13. Canfield, S.G. et al. An isogenic blood-brain barrier model comprising brain endothelial cells, astrocytes, and neurons derived from human induced pluripotent stem cells. *J Neurochem* **140**, 874-888 (2017).

14. Appelt-Menzel, A. et al. Establishment of a Human Blood-Brain Barrier Co-culture Model Mimicking the Neurovascular Unit Using Induced Pluri- and Multipotent Stem Cells. *Stem Cell Reports* **8**, 894-906 (2017).
15. Praça, C. et al. Derivation of Brain Capillary-like Endothelial Cells from Human Pluripotent Stem Cell-Derived Endothelial Progenitor Cells. *Stem Cell Reports* **13**, 599-611 (2019).
16. Stebbins, M.J. et al. Human pluripotent stem cell-derived brain pericyte-like cells induce blood-brain barrier properties. *Sci Adv* **5**, eaau7375 (2019).
17. Qian, T. et al. Directed differentiation of human pluripotent stem cells to blood-brain barrier endothelial cells. *Sci Adv* **3**, e1701679 (2017).
18. Vatine, G.D. et al. Human iPSC-Derived Blood-Brain Barrier Chips Enable Disease Modeling and Personalized Medicine Applications. *Cell Stem Cell* **24**, 995-1005.e1006 (2019).
19. Park, T.E. et al. Hypoxia-enhanced Blood-Brain Barrier Chip recapitulates human barrier function and shuttling of drugs and antibodies. *Nat Commun* **10**, 2621 (2019).
20. Linville, R.M. et al. Human iPSC-derived blood-brain barrier microvessels: validation of barrier function and endothelial cell behavior. *Biomaterials* **190-191**, 24-37 (2019).
21. Nishihara, H. et al. Advancing human induced pluripotent stem cell-derived blood-brain barrier models for studying immune cell interactions. *Faseb j* **34**, 16693-16715 (2020).
22. Cecchelli, R. et al. A stable and reproducible human blood-brain barrier model derived from hematopoietic stem cells. *PLoS One* **9**, e99733 (2014).
23. Mossu, A. et al. A silicon nanomembrane platform for the visualization of immune cell trafficking across the human blood-brain barrier under flow. *J Cereb Blood Flow Metab* **39**, 395-410 (2019).
24. Deligne, C. et al. Development of a human in vitro blood-brain tumor barrier model of diffuse intrinsic pontine glioma to better understand the chemoresistance. *Fluids Barriers CNS* **17**, 37 (2020).
25. Moya, E.L.J. et al. Miniaturization and Automation of a Human In Vitro Blood-Brain Barrier Model for the High-Throughput Screening of Compounds in the Early Stage of Drug Discovery. *Pharmaceutics* **13** (2021).
26. Lippmann, E.S., Azarin, S.M., Palecek, S.P. & Shusta, E.V. Commentary on human pluripotent stem cell-based blood-brain barrier models. *Fluids Barriers CNS* **17**, 64 (2020).
27. Lu, T.M. et al. Pluripotent stem cell-derived epithelium misidentified as brain microvascular endothelium requires ETS factors to acquire vascular fate. *Proc Natl Acad Sci U S A* **118** (2021).
28. Armulik, A. et al. Pericytes regulate the blood-brain barrier. *Nature* **468**, 557-561 (2010).
29. Daneman, R., Zhou, L., Kebede, A.A. & Barres, B.A. Pericytes are required for blood-brain barrier integrity during embryogenesis. *Nature* **468**, 562-566 (2010).
30. Sweeney, M.D., Ayyadurai, S. & Zlokovic, B.V. Pericytes of the neurovascular unit: key functions and signaling pathways. *Nat Neurosci* **19**, 771-783 (2016).
31. Janzer, R.C. & Raff, M.C. Astrocytes induce blood-brain barrier properties in endothelial cells. *Nature* **325**, 253-257 (1987).
32. Simard, M., Arcuino, G., Takano, T., Liu, Q.S. & Nedergaard, M. Signaling at the gliovascular interface. *J Neurosci* **23**, 9254-9262 (2003).
33. Abbott, N.J., Rönnbäck, L. & Hansson, E. Astrocyte-endothelial interactions at the blood-brain barrier. *Nat Rev Neurosci* **7**, 41-53 (2006).
34. Rubin, L.L. et al. A cell culture model of the blood-brain barrier. *J Cell Biol* **115**, 1725-1735 (1991).
35. Wolburg, H. et al. Modulation of tight junction structure in blood-brain barrier endothelial cells. Effects of tissue culture, second messengers and cocultured astrocytes. *J Cell Sci* **107 (Pt 5)**, 1347-1357 (1994).
36. Deli, M.A., Dehouck, M.P., Abrahám, C.S., Cecchelli, R. & Joó, F. Penetration of small molecular weight substances through cultured bovine brain capillary endothelial cell monolayers: the early effects of cyclic adenosine 3',5'-monophosphate. *Exp Physiol* **80**, 675-678 (1995).

463 37. Stenman, J.M. et al. Canonical Wnt signaling regulates organ-specific assembly and differentiation
464 of CNS vasculature. *Science* **322**, 1247-1250 (2008).
465 38. Daneman, R. et al. Wnt/beta-catenin signaling is required for CNS, but not non-CNS, angiogenesis.
466 *Proc Natl Acad Sci U S A* **106**, 641-646 (2009).
467 39. Vanhollebeke, B. et al. Tip cell-specific requirement for an atypical Gpr124- and Reck-dependent
468 Wnt/β-catenin pathway during brain angiogenesis. *Elife* **4** (2015).
469 40. Liebner, S. et al. Wnt/beta-catenin signaling controls development of the blood-brain barrier. *J Cell*
470 *Biol* **183**, 409-417 (2008).
471 41. Cullen, M. et al. GPR124, an orphan G protein-coupled receptor, is required for CNS-specific
472 vascularization and establishment of the blood-brain barrier. *Proc Natl Acad Sci U S A* **108**, 5759-
473 5764 (2011).
474 42. Zhou, Y. et al. Canonical WNT signaling components in vascular development and barrier formation.
475 *J Clin Invest* **124**, 3825-3846 (2014).
476 43. Paolinelli, R. et al. Wnt activation of immortalized brain endothelial cells as a tool for generating a
477 standardized model of the blood brain barrier in vitro. *PLoS One* **8**, e70233 (2013).
478 44. Weksler, B., Romero, I.A. & Couraud, P.O. The hCMEC/D3 cell line as a model of the human blood
479 brain barrier. *Fluids Barriers CNS* **10**, 16 (2013).
480 45. Laksitorini, M.D., Yathindranath, V., Xiong, W., Hombach-Klonisch, S. & Miller, D.W. Modulation
481 of Wnt/β-catenin signaling promotes blood-brain barrier phenotype in cultured brain endothelial
482 cells. *Sci Rep* **9**, 19718 (2019).
483 46. Gastfriend, B.D. et al. Wnt signaling mediates acquisition of blood-brain barrier properties in naïve
484 endothelium derived from human pluripotent stem cells. *Elife* **10** (2021).
485 47. Roudnicky, F. et al. Inducers of the endothelial cell barrier identified through chemogenomic
486 screening in genome-edited hPSC-endothelial cells. *Proc Natl Acad Sci U S A* **117**, 19854-19865
487 (2020).
488 48. Yamashita, M., Aoki, H., Hashita, T., Iwao, T. & Matsunaga, T. Inhibition of transforming growth
489 factor beta signaling pathway promotes differentiation of human induced pluripotent stem cell-
490 derived brain microvascular endothelial-like cells. *Fluids Barriers CNS* **17**, 36 (2020).
491 49. Greene, C., Hanley, N. & Campbell, M. Claudin-5: gatekeeper of neurological function. *Fluids*
492 *Barriers CNS* **16**, 3 (2019).
493 50. Vanlandewijck, M. et al. A molecular atlas of cell types and zonation in the brain vasculature. *Nature*
494 **554**, 475-480 (2018).
495 51. Guérit, S. et al. Astrocyte-derived Wnt growth factors are required for endothelial blood-brain barrier
496 maintenance. *Prog Neurobiol* **199**, 101937 (2021).
497 52. Sabbagh, M.F. et al. Transcriptional and epigenomic landscapes of CNS and non-CNS vascular
498 endothelial cells. *Elife* **7** (2018).
499 53. Yang, A.C. et al. A human brain vascular atlas reveals diverse mediators of Alzheimer's risk. *Nature*
500 **603**, 885-892 (2022).
501 54. Garcia, F.J. et al. Single-cell dissection of the human brain vasculature. *Nature* **603**, 893-899 (2022).
502 55. Fridén, M. et al. Structure-brain exposure relationships in rat and human using a novel data set of
503 unbound drug concentrations in brain interstitial and cerebrospinal fluids. *J Med Chem* **52**, 6233-
504 6243 (2009).
505 56. Sato, S., Matsumiya, K., Tohyama, K. & Kosugi, Y. Translational CNS Steady-State Drug
506 Disposition Model in Rats, Monkeys, and Humans for Quantitative Prediction of Brain-to-Plasma
507 and Cerebrospinal Fluid-to-Plasma Unbound Concentration Ratios. *Aaps j* **23**, 81 (2021).
508 57. Nakagawa, S. et al. A new blood-brain barrier model using primary rat brain endothelial cells,
509 pericytes and astrocytes. *Neurochem Int* **54**, 253-263 (2009).
510 58. Workman, M.J. & Svendsen, C.N. Recent advances in human iPSC-derived models of the blood-
511 brain barrier. *Fluids Barriers CNS* **17**, 30 (2020).

512 59. Linville, R.M. & Searson, P.C. Next-generation in vitro blood-brain barrier models: benchmarking
513 and improving model accuracy. *Fluids Barriers CNS* **18**, 56 (2021).
514 60. Lu, T.M. et al. Human Induced Pluripotent Stem Cell-Derived Brain Endothelial Cells: Current
515 Controversies. *Front Physiol* **12**, 642812 (2021).
516 61. Dehouck, M.P., Méresse, S., Delorme, P., Fruchart, J.C. & Cecchelli, R. An easier, reproducible, and
517 mass-production method to study the blood-brain barrier in vitro. *J Neurochem* **54**, 1798-1801
518 (1990).
519 62. Roudnicky, F. et al. Identification of a combination of transcription factors that synergistically
520 increases endothelial cell barrier resistance. *Sci Rep* **10**, 3886 (2020).
521 63. Santa-Maria, A.R. et al. Flow induces barrier and glycocalyx-related genes and negative surface
522 charge in a lab-on-a-chip human blood-brain barrier model. *J Cereb Blood Flow Metab* **41**, 2201-
523 2215 (2021).
524 64. Linville, R.M. et al. Three-dimensional microenvironment regulates gene expression, function, and
525 tight junction dynamics of iPSC-derived blood-brain barrier microvessels. *Fluids Barriers CNS* **19**,
526 87 (2022).
527 65. Choi, J.-W., Youn, J., Kim, D.S. & Park, T.-E. Human iPS-derived blood-brain barrier model
528 exhibiting enhanced barrier properties empowered by engineered basement membrane. *Biomaterials*
529 **293**, 121983 (2023).

530 Materials and methods

531 Derivation and culture of human stem cell-derived endothelial cells

532 $CD34^+$ hematopoietic stem cells were isolated from human umbilical cord blood and differentiated
533 towards the endothelial lineage as previously described[22]. In accordance with the World Medical
534 Association Declaration of Helsinki, informed consent was obtained from the donors' parents and the
535 protocol was approved by the French Ministry of Higher Education and Research (reference no.
536 CODECOH DC2011-1321). Endothelial cells (ECs) were derived from $CD34^+$ stem cells in
537 endothelial cell growth medium (EGM; Lonza cat# CC-3162) supplemented with 20% fetal calf
538 serum (FCS; Sigma-Aldrich cat# F7524) and 50 ng/mL vascular endothelial growth factor ($VEGF_{165}$;
539 PeproTech, cat# 100-20). After differentiation, ECs were cultured in endothelial cell culture medium
540 (ECM; ScienCell, cat# 1001) supplemented with 5% fetal bovine serum (FBS; Sigma-Aldrich,
541 cat# F4135), 1% endothelial cell growth supplement (ECGS; ScienCell, cat# 1052) and 50 µg/mL
542 gentamicin (Sigma-Aldrich, cat# G1397). For experiments, ECs (passage number 6-7) were either
543 grown in co-culture with or received conditioned medium from bovine brain pericytes (PCs) to
544 acquire brain-like properties, as described in detail below. Cells were kept in a humidified incubator
545 at 37 °C with 5% CO_2.

546 Impedance-based measurement of barrier integrity

547 Real-time, label-free measurement of barrier integrity was performed in 96-well plates with integrated
548 gold electrodes (E-plate 96; Agilent, cat# 300600910) using an xCELLigence RTCA SP device
549 (Agilent). Plates were coated with 0.2% gelatin (Sigma-Aldrich, cat# G2500) and the cell-free
550 background was measured in culture medium for each well. Then, ECs were seeded in the plates at a

551 density of 6×10^3 cells/well and grown until fully confluent, while receiving 50% PC-conditioned
552 medium to acquire brain-like properties. Confluent monolayers were treated with 8-(4-
553 chlorophenylthio)adenosine 3′,5′-cyclic monophosphate sodium salt (cPT-cAMP; Sigma-Aldrich,
554 cat# C3912, 25-250 µM) Ro 20-1724 (Sigma-Aldrich, cat# 557502, 17.5 µM), recombinant human
555 Wnt-3a protein (R&D, cat# 5036-WN, 10-300 ng/mL), recombinant human Wnt-7a protein
556 (PeproTech, cat# 120-31, 10-300 ng/mL), lithium chloride (LiCl; Sigma-Aldrich, cat# L9650,
557 3-30 mM), RepSox (PeproTech, cat# 4463325, 1-30 µM), A83-01 (PeproTech, cat# 9094360,
558 0.1-3 µM) and the impedance of monolayers was measured at 10 kHz at every 5 min for 48-96 h. For
559 combinatorial treatments, the following concentrations were used: cAMP 250 µM, Ro 17.5 µM,
560 Wnt-3a 300 ng/mL, Wnt-7a 300 ng/mL, LiCl 3 mM, RepSox 10 µM and A83-01 3 µM. For all further
561 experiments on human ECs, cARLA treatment consisted of 250 µM cAMP + 17.5 µM Ro + 3 mM
562 LiCl + 3 µM A83-01. The readout of impedance measurements is cell index, a dimensionless
563 parameter which correlates with the strength of cell-cell contacts and cell adhesion. Cell index was
564 defined as $Z_n–Z_0$, where Z_n is the impedance at time point n and Z_0 is the impedance of the cell-free
565 background in each well. Cell index values were normalized to the last time point before treatment.

566 **Construction of the co-culture BBB model**

567 Primary bovine brain PCs were isolated, transfected and maintained as previously described[22].
568 PCs were initially cultured in 0.2% gelatin-coated 100 mm Petri dishes in Dulbecco's Modified Eagle
569 Medium (DMEM; Gibco, cat# 11885084) supplemented with 20% FBS (Sigma-Aldrich, cat# F4135),
570 1% GlutaMAX (Gibco, cat# 35050061) and 50 µg/mL gentamicin (Sigma-Aldrich, cat# G1397).
571 PC-conditioned medium from 48 h cultures was sterile-filtered (0.2 µm) and used in a 1:1 ratio with
572 EC medium to promote the acquisition of brain-like EC properties in experiments where co-culture
573 was not suitable. For all other experiments, a contact co-culture BBB model was used. PCs were
574 gently trypsinized and seeded at the bottom side of collagen IV-coated (Sigma-Aldrich, cat# C5533,
575 100 µg/mL) Transwell inserts (Corning, cat# 3401 (12 mm inserts) and 3413 (6.5 mm inserts),
576 polycarbonate membrane, 0.4 µm pore size) at a density of 1.8×10^4 cells/cm^2. PCs were allowed to
577 attach to the bottom side of the insert (turned upside down) for 3 h at 37 °C, then the insert was placed
578 in a 12 or 24-well plate containing EC medium. ECs were then seeded to the other, collagen IV
579 (100 µg/mL) and fibronectin-coated (Sigma-Aldrich, cat# F1141, 25 µg/mL) side of the insert at a
580 density of 7×10^4 cells/cm^2 in EC medium. 48 h after the assembly of the co-culture, medium was
581 replaced in both compartments. Four days after the assembly of the co-culture, medium was replaced
582 in the bottom compartment and the upper, luminal ('blood side') compartment was treated with
583 control EC medium or cARLA or its constituents for 48 h. Experiments were performed 6 days after
584 the assembly of the co-culture and after 48-h treatment with molecules or their combinations.

585 **Transendothelial electrical resistance**

586 Transendothelial electrical resistance (TEER) was measured first across EC monolayers grown in
587 50% PC-conditioned medium on 6.5 mm Transwell inserts as described above using a CellZScope+

instrument (nanoAnalytics). Confluent monolayers were treated with control medium, cARLA or its components and the impedance spectra of ECs between 1 Hz and 100 KHz was monitored every 3 h over a 96 h period at 37 °C. TEER was automatically calculated by the device and is presented in arbitrary units relative to baseline. TEER was also measured across EC-PC co-cultures using an EVOM voltohmmeter (World Precision Instruments) equipped with a hand-held STX2 chopstick electrode (for 12 mm inserts) or an EndOhm 6G chamber electrode (for 6.5 mm inserts). Electrodes were equilibrated in pre-warmed EC medium for 15 min and TEER was measured on a 37 °C heating pad. TEER in $\Omega \times cm^2$ was calculated by subtracting the mean resistance of two coated, cell-free inserts from raw resistance values, multiplied by the surface area of the insert.

Tracer permeability

After 48 h luminal ('blood side') treatment, the upper, donor compartment of the co-culture model was incubated with tracers sodium fluorescein (376 Da, Sigma-Aldrich, cat# 46960, 10 µg/mL) and Evans blue-albumin complex (67 kDa, 10 mg/mL bovine serum albumin (BSA) + 167.5 µg/mL Evans blue dye) in phenol red-free DMEM/F-12 medium (Gibco, cat# 21041025) supplemented with 1% FBS (Sigma-Aldrich, cat# F4135). Cultures were incubated on a PSU-2T horizontal shaker (Biosan, 150 rpm) for 1 h at 37 °C. Samples from both compartments were collected and the mean fluorescence of tracers was measured using a Fluorolog 3 spectrofluorometer (Horiba Jobin Yvon) with excitation/emission wavelengths 485/515 nm for sodium fluorescein and 584/663 nm for Evans blue-albumin complex. Concentration of tracers were determined by standard calibration curves. Apparent permeability coefficients (P_{app}) were calculated as previously described[66] using the following equation:

$$P_{app} = \frac{\Delta C_A \times V_A}{C_D \times A \times \Delta t}$$

where C_A is the concentration measured in the acceptor compartment at 1 h, V_A is the volume of the acceptor compartment (1.5 and 0.9 mL for 12 and 6.5 mm inserts, respectively), C_D is the concentration in the donor compartment at 0 h, A is the surface area available for permeability (1.12 and 0.33 cm^2 for 12 and 6.5 mm inserts, respectively) and Δt is the duration of the experiment (1 h).

Immunocytochemistry and image analysis

After 48 h luminal ('blood side') treatment, the medium was removed from culture inserts and ECs were fixed with a 1:1 mixture of ice cold methanol-acetone solution for 2 min (for claudin-5, ZO-1 and VE-cadherin staining) or with 3% paraformaldehyde for 15 min at room temperature. Cells were blocked with 3% BSA in phosphate-buffered saline (PBS; KCl 2.7 mM, KH_2PO_4 1.5 mM, NaCl 136 mM, $Na_2HPO_4 \times 2\ H_2O$ 6.5 mM, pH 7.4) for 1 h at room temperature and were subsequently incubated with primary antibodies rabbit anti-claudin-5 (Sigma-Aldrich, cat# SAB4502981, AB_10753223, 1:300), rabbit anti-ZO-1 (Invitrogen, cat# 61-7300, AB_2533147, 1:400), rabbit anti-caveolin-1 (Santa-Cruz, cat# sc-894, AB_2072042, 1:100), mouse anti-P-glycoprotein (Sigma-Aldrich, cat# 517310, AB_564389, 1:100), rabbit anti-β-catenin (Sigma-Aldrich, cat# C2206,

624 AB_476831, 1:200) and rabbit anti-VE-cadherin (Invitrogen, cat# PA519612, AB_10979589, 1:200)
625 diluted in 3% BSA-PBS overnight at 4 °C. For intracellular antigens (F-actin, caveolin-1 and nuclear
626 β-catenin), a permeabilization step with 0.2% Triton X-100 in PBS for 10 min at room temperature
627 preceded blocking. Cells were then incubated with secondary antibodies Alexa Fluor 488 goat anti-
628 rabbit IgG (Thermo Fisher, cat# A-11008, AB_143165, 1:400), Alexa Fluor 555 goat anti-rabbit IgG
629 (Thermo Fisher, cat# A-21428, AB_2535849, 1:400) and Alexa Fluor 647 goat anti-mouse IgG
630 (Thermo Fisher, cat# A-21235, AB_2535804, 1:300), the F-actin probe Alexa Fluor 488 phalloidin
631 (Invitrogen, cat# A12379, 1:100) and the nuclear counterstain Hoechst 33342 (Thermo Fisher,
632 cat# H1399, 1 µg/mL) diluted in PBS for 1 h at room temperature, protected from light. Between each
633 step, cells were washed three times in PBS. Inserts were mounted on glass slides with Fluoromount-
634 G (Southern Biotech, cat# 0100-01) and were examined using a Leica TCS SP5 AOBS confocal laser
635 scanning microscope (Leica Microsystems) equipped with HC PL APO 20× (NA=0.7) and HCX PL
636 APO 63× oil (NA=1.4) objectives. Z-stacks with approximately 0.75 µm spacing were acquired.
637 Maximum intensity projections of each channel were analyzed using the 'Mean gray value' function
638 in Fiji (ImageJ) software by an observer blinded to the experimental groups. Claudin-5 relative
639 continuity was quantified in MATLAB software (The Mathworks Incorporated). For that, images
640 were first corrected for intensity inhomogeneities by a normalized two-dimensional cross-correlation
641 (*normxcorr2*) run with a gaussian template of 2 pixel variance approximating the point spread
642 function of the microscope. Then, image masks corresponding to junctional regions were determined
643 by thresholding the corrected and normalized images with a threshold value of 0.25. Finally, the
644 fragmentation of junctional regions was quantified by calculating the ratio of the total number
645 of distinct regions in the mask to the total masked area. Continuity was defined as the reciprocal of
646 fragmentation or simply the mean size of distinct regions in the image masks. β-catenin
647 nuclear/non-nuclear ratio was also determined using MATLAB software. Areas corresponding to
648 nuclear and cytoplasmic staining were determined by a simple threshold-based segmentation carried
649 out on images of Hoechst 33342-stained nuclei of the same Z-stacks. Using the obtained segmentation
650 masks, mean fluorescence pixel intensity of β-catenin staining was calculated for areas corresponding
651 to the nuclei and cytoplasm.

652 **Total RNA isolation**

653 Human stem cell-derived brain-like ECs (in co-culture with PCs) were grown on Transwell inserts
654 (Corning, cat# 3401) for 6 days. For the last 48 hours, ECs were treated luminally with cARLA or
655 control medium containing the amount of solvents (Milli-Q water 100× and DMSO 1000× dilution)
656 corresponding to cARLA. After treatment, PCs were removed and ECs were lysed directly with
657 Buffer RLT Plus (Qiagen, cat# 1053393) on the inserts. For 1 sample in further analyses, cell lysates
658 from 2 inserts were pooled. RNA was isolated using RNeasy Plus Micro Kit (Qiagen, cat# 74034)
659 containing an integrated gDNA eliminator spin column according to the manufacturer's protocol.
660 RNA integrity was analyzed using automated capillary electrophoresis (RNA Pico Sensitivity Assay,
661 LabChip GX II Touch HT instrument, Perkin Elmer). Samples were stored at -80 °C until further
662 analysis.

663 **Library preparation and 3' RNA-sequencing (MACE-seq)**

664 Genome-wide gene expression profiling was performed by massive analysis of cDNA ends (MACE-
665 seq). For library preparation, samples with 1 µg of purified RNA were used. A total of 8 libraries
666 (4 control and 4 cARLA) were constructed using the Rapid MACE-Seq kit (GenXPro GmbH,
667 Frankfurt, Germany) according to the manufacturer's protocol. Fragmented RNA was reverse
668 transcribed into cDNA, using barcoded oligo(dT) primers containing TrueQuant unique molecular
669 identifiers, followed by template switching. Library amplification was done using polymerase chain
670 reaction (PCR), purified by solid phase reversible immobilization beads (Agencourt AMPure XP,
671 Beckman Coulter, cat# A63882). Sequencing was performed on an Illumina NextSeq 500 platform.

672 **Bioinformatic analysis of MACE-seq data**

673 Approximately 58 million single 75 bp MACE-seq reads were obtained across all 8 libraries. PCR
674 duplicates were identified using TrueQuant technology and were removed from raw data.
675 The remaining reads were further poly(A)-trimmed and low-quality reads were discarded. Clean
676 reads were then aligned to the human reference genome (hg38, http://genome.ucsc.edu/cgi-
677 bin/hgTables) using the Bowtie2 mapping tool[67], resulting in a dataset of 21,691 genes. Gene count
678 data was normalized to account for differences in library size and RNA composition bias by
679 calculating the median of gene expression ratios using the DESeq2 R/Bioconductor package[68].
680 Testing for differential gene expression was also performed using DESeq2. As a result, *P*-value and
681 $\log_2$FC ($\log_2$[fold change]) were obtained for each gene in the dataset. To account for multiple
682 comparisons, false discovery rate (FDR) was calculated using the Benjamini-Hochberg method.
683 Genes with an FDR < 0.01 and $|\log_2 FC| > 0.2$ were considered to be differentially expressed.
684 To perform functional enrichment analysis of up- and downregulated gene sets upon cARLA
685 treatment, the g:GOSt tool in g:Profiler[69] was used to identify over-represented Gene Ontology
686 Biological Process (GO:BP) terms and to calculate gene ratios and statistical significance for each
687 pathway. Heatmaps were created by calculating row z-scores for each gene using Min-Max scaling
688 on normalized counts with the following formula:

689 $$\text{Row z-score} = \frac{\text{Value} - \text{Row min}}{\text{Row max} - \text{Row min}}$$

690 **Glycocalyx staining and measurement of cell surface charge**

691 After 48 h luminal ('blood side') treatment with cARLA or control medium, PCs were removed from
692 culture inserts, ECs were washed in PBS and fixed with 1% paraformaldehyde for 15 min at room
693 temperature. Cells were then incubated with Alexa Fluor 488-conjugated wheat germ agglutinin
694 (WGA) lectin (Invitrogen, cat# W11261, 5 mg/mL, 10 min at room temperature) that labels sialic
695 acid and N-acetyl-D-glucosamine residues in the EC glycocalyx. Hoechst 33342 (Thermo Fisher,
696 cat# H1399, 1 µg/mL) was used to counterstain nuclei. Cells were washed in PBS, mounted on glass
697 slides with Fluoromount-G (Southern Biotech, cat# 0100-01) and were examined using a Leica TCS
698 SP5 AOBS confocal laser scanning microscope equipped with a HCX PL APO 63× oil (NA=1.4)

699 objective exactly as described above. Maximum intensity projections of Z-stacks from each channel
700 were analyzed using the 'Mean gray value' function in Fiji (ImageJ) software by an observer blinded
701 to the experimental groups. For the measurement of EC surface charge, EC-PC co-cultures were
702 established exactly as described above, but on transparent Transwell inserts (Corning, cat# 3460,
703 PET, 0.4 µm pore size) to be able to monitor the de-attachment of cells from the inserts. After 48 h
704 treatment, ECs were washed with Ringer-HEPES solution (118 mM NaCl, 4.8 mM KCl, 2.5 mM
705 $CaCl_2$, 1.2 mM $MgSO_4$, 5.5 mM D-glucose, 20 mM HEPES, pH 7.4), gently trypsinized and
706 centrifuged at 700×*g* for 5 min. The cell pellet was resuspended in PBS supplemented with Ca^{2+} and
707 Mg^{2+} ($CaCl_2 \times 2H_2O$ 1.2 mM, $MgCl_2 \times 6H_2O$ 0.5 mM) and zeta potential of 10^5 cells per cuvette was
708 measured using a Zetasizer Nano ZS instrument (Malvern) equipped with a He-Ne laser (λ=632.8 nm)
709 as previously described[63]18.

710 **Albumin internalization**

711 ECs were cultured in 50% PC-conditioned medium on 35 mm glass bottom Petri dishes (Greiner
712 Bio-One, cat# 627860) coated with collagen IV (Sigma-Aldrich, cat# C5533, 100 µg/mL) and
713 fibronectin (Sigma-Aldrich, cat# F1141, 25 µg/mL) at a seeding density of 5×10^4 cells/cm^2. Confluent
714 monolayers were treated with cARLA or control medium for 48 h. After that, culture medium was
715 removed and cells were incubated with Texas Red-conjugated BSA (TR-albumin; Invitrogen,
716 cat# A23017, 5 µg/mL) dissolved in control medium for 2 h at 37 °C. For the final 20 minutes of
717 incubation, Hoechst 33342 (Thermo Fisher, cat# H1399, 2 µg/mL) was added to cells to counterstain
718 nuclei. Cultures were washed twice in Ringer-HEPES supplemented with 1% FBS and live-cell
719 imaging was performed immediately in the same buffer using a Leica TCS SP5 AOBS confocal laser
720 scanning microscope equipped with a HCX PL APO 63× oil (NA=1.4) objective with the same
721 parameters as described above. After live-cell imaging, cells were fixed with 3% paraformaldehyde
722 for 15 min at room temperature and immunostained for caveolin-1 exactly as described above.
723 YZ and XZ projections of Z-stacks were generated in the LAS X software (Leica Microsystems,
724 version 3.7.5) to visualize TR-albumin and caveolae. For measuring albumin internalization under
725 inhibitory conditions, cells were cultured in 50% PC-conditioned medium in 24-well plates
726 (Corning, cat# CLS3527, flat-bottom) coated with collagen IV and fibronectin at a seeding density
727 of 1.6×10^4 cells/cm^2. Confluent monolayers were treated with cARLA or control medium for 48 h.
728 To inhibit lipid raft/caveolin-mediated endocytosis, methyl-β-cyclodextrin (MβCD; Sigma-Aldrich,
729 cat# C4555, 1 mM) was added to the medium of some groups for 1 h at 37 °C. Cells were then
730 incubated with TR-albumin diluted in control EC medium containing 1% FBS for 2 h at 37 or 4°C.
731 After that, cells were washed three times with ice cold PBS supplemented with 0.1% BSA, once with
732 acid stripping buffer (glycine 50 mM, NaCl 100 mM, pH 3.0) to remove cell surface-associated
733 TR-albumin and once with PBS. Finally, ECs were lysed with 1% Triton X-100 in Milli-Q water and
734 the fluorescent signal of internalized TR-albumin was quantified with a Fluorolog 3
735 spectrofluorometer (Horiba Jobin Yvon) at 592 nm excitation and 612 nm emission wavelengths.
736 Concentrations of internalized TR-albumin were calculated using a standard calibration curve.

737 Values were normalized for total protein content in each well using a Pierce BCA Protein Assay Kit
738 (Thermo Fisher, cat# 23225) according to the manufacturer's instructions.

739 **Efflux pump activity**

740 After 48 h luminal ('blood side') treatment with cARLA or control medium, the permeability of
741 rhodamine 123, a ligand of efflux pumps, was measured across the co-culture model in blood-to-brain
742 (A-B) and brain-to-blood (B-A) directions. Either the luminal or abluminal ('brain side')
743 compartment of the model was incubated with rhodamine 123 (Sigma-Aldrich, cat# R83702, 10 µM)
744 diluted in phenol red-free DMEM/F-12 medium (Gibco, cat# 21041025) supplemented with 1% FBS
745 (Sigma-Aldrich, cat# F4135) for 1 h at 37 °C on a horizontal shaker set to 150 rpm. To block efflux
746 pump activity in some of the groups, verapamil (Sigma-Aldrich, cat# V4629, 2 µM) was added to the
747 luminal compartment 30 minutes prior to rhodamine 123 treatment. After 1 h, samples from both
748 compartments were collected and the mean fluorescence of rhodamine 123 was measured using a
749 Fluorolog 3 spectrofluorometer (Horiba Jobin Yvon) with excitation/emission wavelengths
750 492/526 nm. Concentrations of rhodamine 123 were determined by standard calibration curves.
751 Apparent permeability coefficients (P_{app}) were calculated as described above. Efflux ratio reflecting
752 appropriate polarity of efflux pumps was calculated by dividing P_{app} values in B-A direction by P_{app}
753 values in A-B direction.

754 **Pharmacological inhibition of Wnt/β-catenin signaling**

755 Wnt/β-catenin signaling was blocked at two different points using inhibitors ICG-001
756 (MedChemExpress, cat# HY-14428) and XAV 939 (MedChemExpress, cat# HY-15147). For the
757 measurement of barrier integrity by impedance, ECs were cultured as described above. Confluent
758 monolayers were treated with ICG-001 (5-50 µM) or XAV 939 (0.5-3 µM) for 48 h at 37 °C, and
759 impedance was measured at 10 kHz every 5 min using the xCELLigence RTCA SP device (Agilent)
760 as described above. To investigate how the effect of cARLA is modulated by these inhibitors, ECs
761 were co-treated with cARLA and either 5 µM ICG-001 or 1 µM XAV 939 for 48 h at 37 °C. For the
762 measurement of TEER and tracer permeability, EC-PC co-cultures were assembled and maintained
763 as described above. On day 4, the luminal (blood) side of the model was incubated with cARLA or
764 control medium supplemented with either 5 µM ICG-001 or 1 µM XAV 939 for 48 h at 37 °C.
765 TEER and tracer permebility were then measured and calculated as described above.

766 **Penetration of small molecule drugs across the BBB model**

767 The penetration of ten selected small molecule drugs (atenolol, indomethacin, lamotrigine,
768 loperamide, methotrexate, propranolol, salicylic acid, tacrine, verapamil and vinblastine) was
769 measured in blood-to-brain (A-B) and brain-to-blood (B-A) directions across the EC-PC co-culture
770 model. Properties and catalog numbers of drugs are listed in **Supplementary Table 1**. Assembly,
771 maintainance and treatment of co-cultures were performed as described above. After 48 h cARLA

or control treatment, either the luminal (blood) or abluminal (brain) compartment of the model was incubated with 1 µM of drug compounds (stocks of 10 mM were prepared in DMSO) diluted in Ringer-HEPES solution (118 mM NaCl, 4.8 mM KCl, 2.5 mM $CaCl_2$, 1.2 mM $MgSO_4$, 5.5 mM D-glucose, 20 mM HEPES, pH 7.4) supplemented with 0.1% FBS (Sigma-Aldrich, cat# F4135) at 37 °C on a horizontal shaker set to 150 rpm. In B-A direction, samples from both compartments were collected at 60 min. In A-B direction, inserts were transferred to a new well with fresh buffer at 30 min, then at the end of the assay samples were collected from the donor (0-60 min) and acceptor compartments (0-30 min, 30-60 min). Samples were precipitated with -20 °C methanol (Molar Chemicals, cat# 05730-101-340) and drug content was measured using a Sciex API 4000 MS-Agilent 1260 Infinity UHPLC instrumental setup, except for methotrexate, which was measured using a Sciex x500r QTOF MS - Exion LC setup. Measurement parameteres are listed in **Supplementary Table 2**. Drug concentrations were determined by standard calibration curves. To calculate apparent permeability coefficients (P_{app}) using multiple timepoints, clearance was first calculated[57,66]:

$$\text{Clearance } (\mu L) = \frac{C_A \times V_A}{C_D}$$

where C_A is the concentration measured in the acceptor compartment, V_A is the volume of the acceptor compartment (1.5 mL) and C_D is the treatment concentration in the donor compartment at a given timepoint. Cumulative clearance values were plotted against time at 0, 30 and 60 min and a simple linear regression was used to calculate clearance rate (PS_t; µL/min) as the slope of the curve. P_{app} was then calculated as:

$$P_{app} = \frac{PS_t}{A}$$

where A is the surface area of the insert available for permeability (1.12 cm^2). Efflux ratio was calculated by dividing P_{app} values in B-A direction by P_{app} values in A-B direction. To calculate the *in vitro* unbound brain-to-plasma partition coefficients ($K_{p,uu,brain}$)[22,25,55] of drugs in the A-B direction, recovery for each compound was first calculated as:

$$R = \frac{n_{A,30} + n_{A,60} + n_{D,60}}{n_T}$$

where $n_{A,30}$, $n_{A,60}$ and $n_{D,60}$ are the amounts of substance (pmol) in the acceptor compartment at 30- and 60 min as well as the donor compartment at 60 min, respectively, and n_T is the amount of substance (pmol) present at the treatment solution at 0 min. *In vitro* $K_{p,uu,brain}$ was then calculated as:

$$K_{p,uu,brain} = \frac{C_T - C_D}{C_D} \times R$$

where C_T is the concentration of a drug in the treatment solution at 0 min, C_D is the concentration in the donor compartment at 60 min and R is recovery. Calculation of Pearson r^2 and Spearman r coefficients using data referenced in the legend Fig. 5d was performed in GraphPad Prism software (version 5.0).

Synthesis and penetration of nanoparticles across the BBB model

Poly(L-glutamic acid) nanoparticles (NPs) were synthesized as previously described[70]. As a targeting ligand for penetration across the BBB, reduced L-glutathione was added to NPs *via* the EDC/NHS

808 coupling reaction in a molar ratio of L-glutamic acid:L-glutathione=2:1. NPs were grafted with *N*-(2-
809 aminoethyl) rhodamine 6G-amide bis(trifluoroacetate) (rhodamine 6G) *via* EDC/NHS coupling in a
810 weight ratio of NP:rhodamine 6G=1:20 to fluorescently label the particles. Assembly, maintainance
811 and treatment of BBB co-cultures were performed as described above. After 48 h cARLA or control
812 treatment, the luminal ('blood side') compartment of the model was incubated with non-targeted
813 or GSH-targeted NPs (50 µg/mL) diluted in phenol red-free DMEM/F-12 medium (Gibco,
814 cat# 21041025) supplemented with 1% FBS (Sigma-Aldrich, cat# F4135) at 37 °C on a horizontal
815 shaker set to 150 rpm. Inserts were transferred to a new well with fresh buffer at 1 h and 4h, then at
816 the end of the assay samples were collected from the donor (0-24 h) and acceptor compartments
817 (0-1 h, 1-4 h, 4-24 h). The mean fluorescence of rhodamine 6G was measured using a Fluorolog 3
818 spectrofluorometer (Horiba Jobin Yvon) with excitation/emission wavelengths 525/-551 nm.
819 NP concentrations were determined by standard calibration curves. To calculate endothelial
820 permeability coefficients (P_e) using multiple timepoints[57], clearance and clearance rate were first
821 calculated as described above for inserts with cells and for blank inserts without cells (PS_{total} and
822 PS_{blank}). The permeability × surface area product value for the endothelial monolayer (PS_e) was
823 calculated using the following formula:

824 $$\frac{1}{PS_e} = \frac{1}{PS_{total}} - \frac{1}{PS_{blank}}$$

825 P_e was then calculated by dividing permeability × surface area product value for the endothelial
826 monolayer by the surface area of the insert available for permeability (1.12 cm^2):

827 $$P_e = \frac{PS_e}{A}$$

828 For the visualization of NP internalization, ECs were grown in 50% PC-conditioned medium on
829 35 mm glass bottom Petri dishes (Greiner Bio-One, cat# 627960) coated with collagen IV
830 (100 µg/mL) and fibronectin (25 µg/mL) at a seeding density of 5×10^4 cells/cm^2. After 48 h treatment
831 with cARLA or control medium, cells were incubated with non-targeted or GSH-targeted NPs
832 (50 µg/mL) diluted in EC medium for 24 h at 37 °C. For the final 20 minutes of incubation,
833 Hoechst 33342 (Thermo Fisher, cat# H1399, 2 µg/mL) was added to cells to counterstain nuclei.
834 Cultures were washed twice in Ringer-HEPES supplemented with 1% FBS and live-cell imaging was
835 performed immediately in the same buffer using a Leica TCS SP5 AOBS confocal laser scanning
836 microscope equipped with a HCX PL APO 63× oil (NA=1.4) objective exactly as described above.

837 **Mouse brain endothelial cell line bEnd.3**

838 The mouse brain endothelial cell line bEnd.3 was purchased from ATCC (cat# CRL-2299) and
839 cultured in DMEM/F-12 medium (Gibco, cat# 11320033) supplemented with 10% FBS
840 (Sigma-Aldrich, cat# F4135) and 50 µg/mL gentamicin (Sigma-Aldrich, cat# G1397). Cells were
841 used between passage numbers 25-28. For the measurement of barrier integrity by impedance, bEnd.3
842 cells were seeded at a density of 6×10^3 cells/well in rat tail collagen-coated (150 µg/mL) 96-well
843 plates (E-plate 96; Agilent, cat# 300600910) and were treated as described above for human ECs.

844 For the measurement of TEER and tracer permeability, bEnd.3 cells were passaged to Transwell
845 inserts (Corning, cat# 3401 and 3413, polycarbonate, 0.4 µm pore size) at a density of
846 6.3×10^4 cells/cm^2 and grown in monoculture for 4 days. After that, bEnd.3 cells were treated from
847 the luminal ('blood side') with cARLA optimized for this cell type (125 µM cAMP + 17.5 µM Ro +
848 10 mM LiCl + 1 µM A83-01) for 48 h at 37 °C. TEER and tracer permeability was measured, and
849 immunocytochemistry for claudin-5 and ZO-1 was performed exactly as described above for
850 human ECs.

851 **Animals**

852 For primary cell isolation, brain tissue was harvested from 3-week-old and newborn Wistar rats
853 (Harlan Laboratories) of both sexes according to the regulations of the 1998. XXVIII. Hungarian law
854 and the EU Directive 2010/63/EU about animal protection and welfare. Animals were housed in a
855 conventional animal facility at the Biological Research Centre, Szeged, Hungary under standard
856 conditions (22–24 °C, 12 h light/dark cycle) with regular rodent chow diet and water available
857 *ad libitum*.

858 **Rat primary endothelial cell-pericyte-astrocyte co-culture BBB model**

859 The isolation of primary rat brain capillary ECs, PCs and ACs was performed as previously
860 described[57]. After isolation, ECs were seeded on 100 mm Petri dishes coated with collagen IV
861 (100 µg/mL) and fibronectin (25 µg/mL) and were cultured in DMEM/F-12 medium (Gibco,
862 cat# 11320033) supplemented with 15% plasma-derived bovine serum (PDS; First Link,
863 cat# 24-00-850), 10 mM HEPES (Sigma-Aldrich, cat# H4034), 1 ng/mL basic fibroblast growth
864 factor (bFGF; Sigma-Aldrich, cat# F0291), 100 µg/mL heparin (Sigma-Aldrich, cat# 43149-100KU),
865 100× Insulin-Transferrin-Selenium reagent (ITS; Gibco, cat# 41400045) and 50 µg/mL gentamicin
866 (Sigma-Aldrich, cat# G1397). During the first 3 days of culture, the medium of ECs also contained
867 3 µg/mL puromycin to eliminate P-glycoprotein negative, contaminating cell types[71]. From day 4,
868 PDS concentration in the medium of ECs was reduced to 10%. For the measurement of barrier
869 integrity by impedance, ECs were seeded at a density of 6×10^3 cells/well in 96-well plates (E-plate 96;
870 Agilent, cat# 300600910) coated with collagen IV (100 µg/mL) and fibronectin (25 µg/mL) and were
871 treated as described above for human ECs. PCs were seeded onto culture dishes coated with collagen
872 IV (100 µg/mL) and were cultured in DMEM (1 g/L glucose, Gibco, cat# 11885084) supplemented
873 with 10% FBS (Sigma-Aldrich, cat# F4135) and 50 µg/mL gentamicin. ACs were seeded into 12-well
874 plates (Corning, cat# 3513) coated with rat tail collagen (150 µg/mL) at a density of 8.5×10^4 cells/cm^2
875 and were cultured in the same medium as PCs. To assemble the triple co-culture model, PCs were
876 passaged to the bottom side of Transwell inserts (Corning, cat# 3401, polycarbonate, 0.4 µm pore
877 size) coated with collagen IV (100 µg/mL) at a density of 1.5×10^4 cells/cm^2. PCs were allowed to
878 attach to the inserts for 3 h at 37 °C, then the insert was placed in a 12-well plate containing the ACs
879 and the medium was replaced to EC medium. ECs were then seeded to the other, upper side of the
880 culture insert coated with collagen IV (100 µg/mL) and fibronectin (25 µg/mL) at a density of

881 7×10^4 cells/cm^2 in EC medium. The three cell types were cultured together for 3-4 days before
882 cARLA treatment. After that, the triple co-culture model was treated from the luminal ('blood side')
883 with cARLA optimized for this cell type (250 µM cAMP + 17.5 µM Ro + 1 mM LiCl + 1 µM A83-01)
884 for 24 h at 37 °C. TEER and tracer permeability was measured, and immunocytochemistry for
885 claudin-5 and ZO-1 was performed exactly as described above for human ECs.

886 **Statistics**

887 Individual wells or inserts of cultured cells that underwent the same experimental procedure are
888 defined as replicates. For immunocytochemistry, individual fields of view (4-5 fields of view per
889 culture insert) are defined as replicates. All key experiments were repeated independently and detailed
890 information about error bars, sample size, replication strategy and statistical tests are provided in each
891 figure legend. Statistical analyses were performed in GraphPad Prism software (version 5.0).
892 Unpaired *t*-test or one-way ANOVA followed by Bonferroni's post-hoc test were used to compare
893 means from two or more groups, respectively, on normally distributed data determined by Shapiro-
894 Wilk test. In experiments with two independent variables, two-way ANOVA with Bonferroni's
895 post-hoc test was used. Statistical significance was set at $P < 0.05$.

896 **References (continued, for Methods)**

897 66. Veszelka, S. et al. Comparison of a Rat Primary Cell-Based Blood-Brain Barrier Model With
898 Epithelial and Brain Endothelial Cell Lines: Gene Expression and Drug Transport. *Front Mol*
899 *Neurosci* **11**, 166 (2018).
900 67. Langmead, B. & Salzberg, S.L. Fast gapped-read alignment with Bowtie 2. *Nat Methods* **9**, 357-
901 359 (2012).
902 68. Love, M.I., Huber, W. & Anders, S. Moderated estimation of fold change and dispersion for
903 RNA-seq data with DESeq2. *Genome Biol* **15**, 550 (2014).
904 69. Raudvere, U. et al. g:Profiler: a web server for functional enrichment analysis and conversions
905 of gene lists (2019 update). *Nucleic Acids Res* **47**, W191-w198 (2019).
906 70. Mészáros, M. et al. Targeting Human Endothelial Cells with Glutathione and Alanine Increases
907 the Crossing of a Polypeptide Nanocarrier through a Blood-Brain Barrier Model and Entry to
908 Human Brain Organoids. *Cells* **12**, 503 (2023).
909 71. Perrière, N. et al. Puromycin-based purification of rat brain capillary endothelial cell cultures.
910 Effect on the expression of blood-brain barrier-specific properties. *J Neurochem* **93**, 279-289
911 (2005).

912 **Data availability**

913 MACE-seq datasets generated and analyzed in this study have been deposited to the Gene Expression
914 Omnibus (GEO) repository under the accession number GSE224846. Source data is provided for
915 all figures.

Acknowledgements and funding

We thank Dr. Imola Wilhelm and Dr. István Krizbai from the Neurovascular Unit Research Group at the Biological Research Centre, Szeged for the use of a CellZScope+ instrument and Dr. Tibor Páli from the Membrane Biophysics Research Group at the Biological Research Centre, Szeged for the use of a Horiba Jobin-Yvon Fluorolog 3 spectofluorometer. We also thank Ildikó Valkonyné Kelemen and Dr. Gábor Steinbach from the Cellular Imaging Laboratory at the Biological Research Centre, Szeged for providing support in microscopy.

This work was funded by the National Research, Development and Innovation Office of Hungary (K143766 for M.A.D.), and the Hungarian Academy of Sciences (NAP2022-I-6/2022). G.P. was supported by the National Academy of Scientist Education Program of the National Biomedical Foundation under the sponsorship of the Hungarian Ministry of Culture and Innovation, the Stephen W. Kuffler Research Foundation, the Gedeon Richter Plc. Centenarial Foundation, and by the New National Excellence Program of the Ministry for Innovation and Technology (ÚNKP-22-3-SZTE-446). M.M. was supported by the the National Research, Development and Innovation Office, Budapest, Hungary (PD138930), the Gedeon Richter Plc. Centenarial Foundation and the "National Talent Program" with the financial aid of the Ministry of Human Resources (NTP-NFTÖ-22-B-0150). A.S. was supported by the New National Excellence Program of the Ministry for Innovation and Technology (ÚNKP-22-3-SZTE-458), and the Gedeon Richter Plc Centenarial Foundation (2022/R/26/2533). J.P.V. was supported by the „National Talent Program" with the financial aid of the Ministry of Human Resources (NTP-NFTÖ-22-B-0229). F.R.W. was supported by the Secretariat of Lorand Eotvos Research Network (SA-111/2021). S.V. was supported by the Premium Postdoctoral Research Program (Premium-2019–469) of the Hungarian Academy of Sciences and by National Research, Development and Innovation Office of Hungary (FK143233).

Author contributions

Conceptualization, G.P. and M.A.D.; Formal Analysis, G.P., M.M., A.S., F.R.W., R.F., I.K. and G.V.; Investigation, G.P., M.M., A.S., J.P.V., F.R.W., R.F., I.K. and S.V.; Resources, R.F., J.S.J., F.G. and M.V.; Writing – Original Draft, G.P. and M.A.D.; Writing – Review & Editing, G.P., M.M., A.S., J.P.V., F.R.W., R.F., I.K., G.V., J.S.J, F.G., M.V., S.V. and M.A.D.; Visualization Preparation, G.P.; Supervision, S.V. and M.A.D.; Project Administration, G.P. and M.A.D.; Funding Acquisition, S.V. and M.A.D.

Competing interests

Authors I.K. and M.V. are employed by the company Gedeon Richter Plc. and R.F. is employed by the company GenXPro GmbH. These authors were blinded to the experimental groups during data collection and analysis. Other authors declare that the research was conducted in the absence of any commercial or financial relationships that could be viewed as a potential conflict of interest.

Extended Data Figures

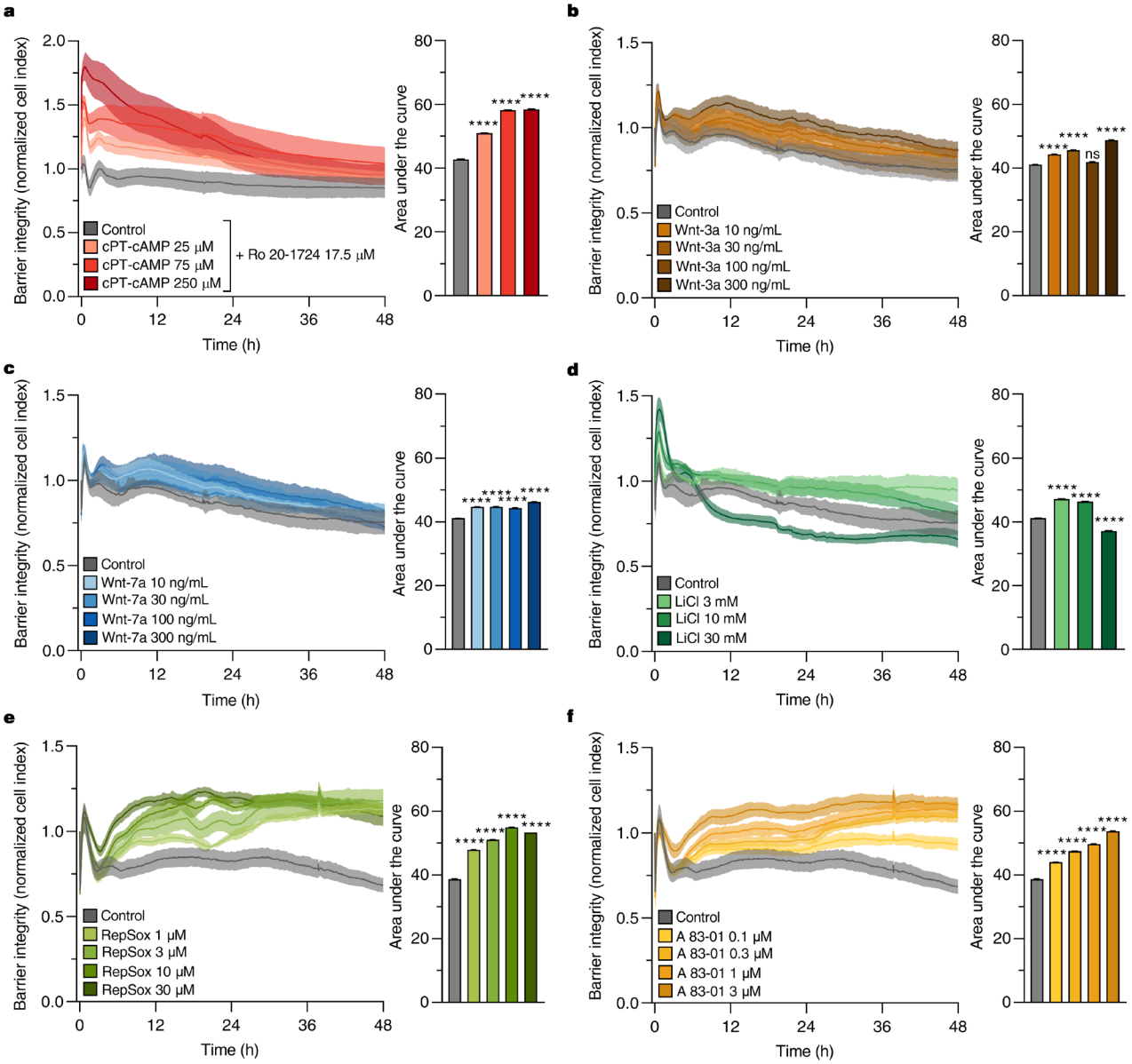

Extended Data Fig. 1. Effect of small molecules and recombinant proteins targeting single pathways in human stem cell-derived ECs on barrier integrity measured by impedance.
Treatment concentrations and durations were optimized for **a)** cPT-cAMP supplemented with the cAMP-specific phosphodiesterase inhibitor Ro 20-1724, **b-d)** activators of Wnt signaling and **e-f)** inhibitors of TGF-β signaling. Selected concentrations for further experiments were: cPT-cAMP 250 µM, Wnt-3a 300 ng/mL, Wnt-7a 300 ng/mL, LiCl 3 mM, RepSox 10 µM and A83-01 3 µM. Higher normalized cell index values and a higher area under the curve indicates increased barrier integrity. Mean ± SD, ANOVA with Bonferroni's post-hoc test, ****P<0.0001, ns: P>0.05 compared to the control group, n=6.

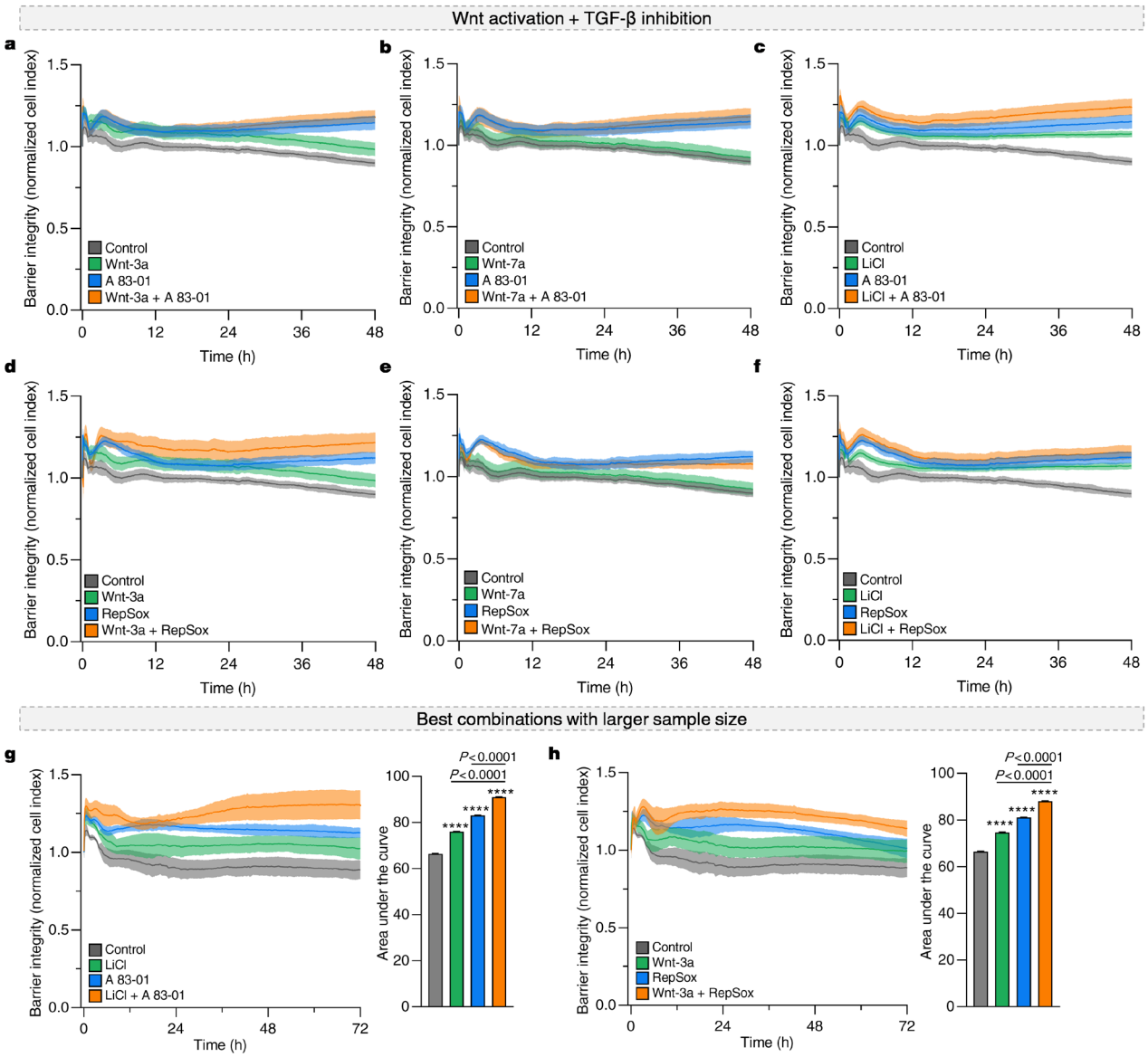

Extended Data Fig. 2. Effect of simultaneous activation of Wnt and inhibition of TGF-β signaling on barrier integrity in human stem cell-derived ECs.

Impedance kinetics of ECs treated with **a-f)** Wnt activators (Wnt-3a 300 ng/mL, Wnt-7a 300 ng/mL, LiCl 3 mM), TGF-β receptor antagonists (RepSox 10 10 μM, A83-01 3 μM) and their combinations. Mean ± SD, *n*=5. **g-h)** The best combinations (LiCl+A83-01, Wnt-3a+RepSox) were also validated with a larger sample size. Higher normalized cell index values and a higher area under the curve indicates increased barrier integrity. Mean ± SD, ANOVA with Bonferroni's post-hoc test, ****$P<0.0001$ compared to the control group, $n=10$.

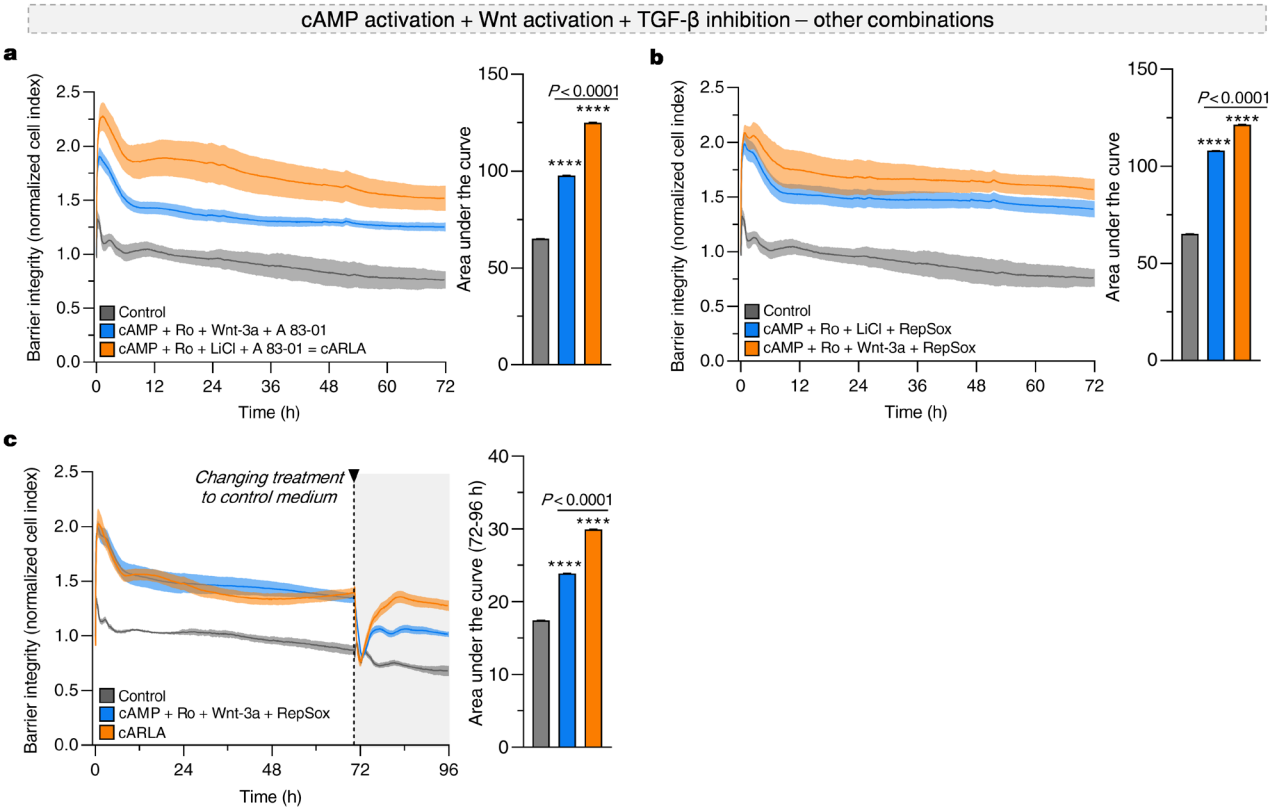

Extended Data Fig. 3. Effect of simultaneous activation of cAMP and Wnt as well as inhibition of TGF-β signaling on barrier integrity in human stem cell-derived ECs.
Impedance kinetics of ECs treated with combinations containing **a)** A83-01 and **b)** RepSox, targeting all three pathways simultanously. The same concentrations of compounds were used as described above. Of note, some combinations (cARLA, cAMP+Ro+Wnt-3a+RepSox) more effectively elevated barrier integrity than others (cAMP+Ro+Wnt-3a+A83-01, cAMP+Ro+LiCl+RepSox). **c)** Impedance kinetics of EC monolayers treated with the two best combinations. Treatment was changed to control medium at 72 h. Of note, cARLA outperformed cAMP+Ro+Wnt-3a+RepSox, since its effect was more resilient to the withdrawal of treatment. This makes cARLA a more suitable candidate to be used in permeability experiments, where the presence of small molecule compounds can potentially interfere with downstream analytics. Higher normalized cell index values and a higher area under the curve indicates increased barrier integrity. Mean ± SD, ANOVA with Bonferroni's post-hoc test, ****P<0.0001 compared to the control group, n=6 for all three panels.

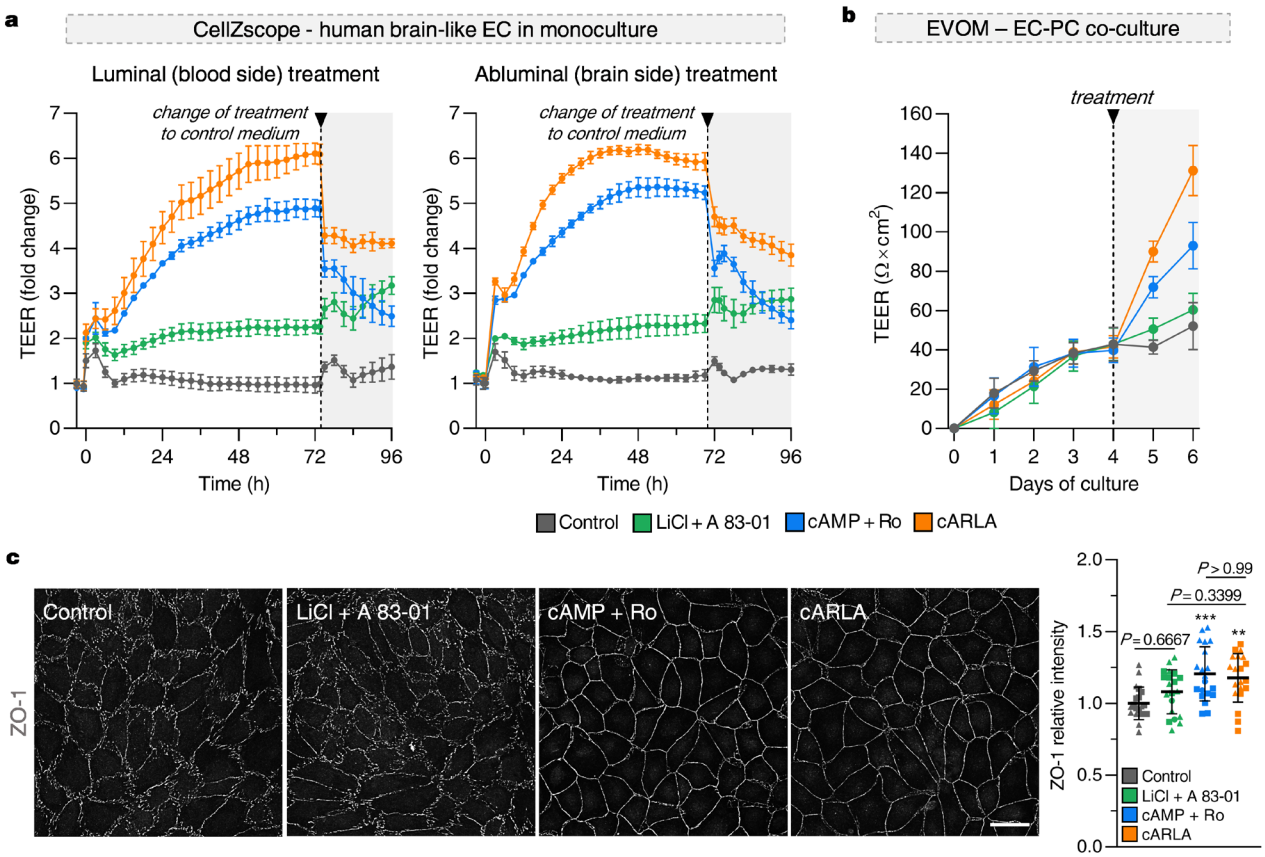

Extended Data Fig. 4. Additional measurements of barrier- and junctional integrity in brain-like ECs. **a)** Automated measurement of transendothelial electrical resistance (TEER) in brain-like ECs after treatment with cARLA or its components using the cellZscope instrument. Luminal and abluminal treatment was only applied for compounds LiCl and A83-01. Compounds cAMP+Ro were always administered luminally. **b)** Manual measurement of TEER across the EC-PC co-culture model over time using an EVOM voltohmmeter and hand-held STX-2 electrodes. **c)** Immunostaining of the tight junction protein ZO-1 in ECs from the co-culture model after 48 h treatment. Bar: 50 µm. Quantification: Mean ± SD, ANOVA with Bonferroni's post-hoc test, $^{**}P<0.01$, $^{***}P<0.001$ compared to the control group, n=20-21 from 2 independent experiments.

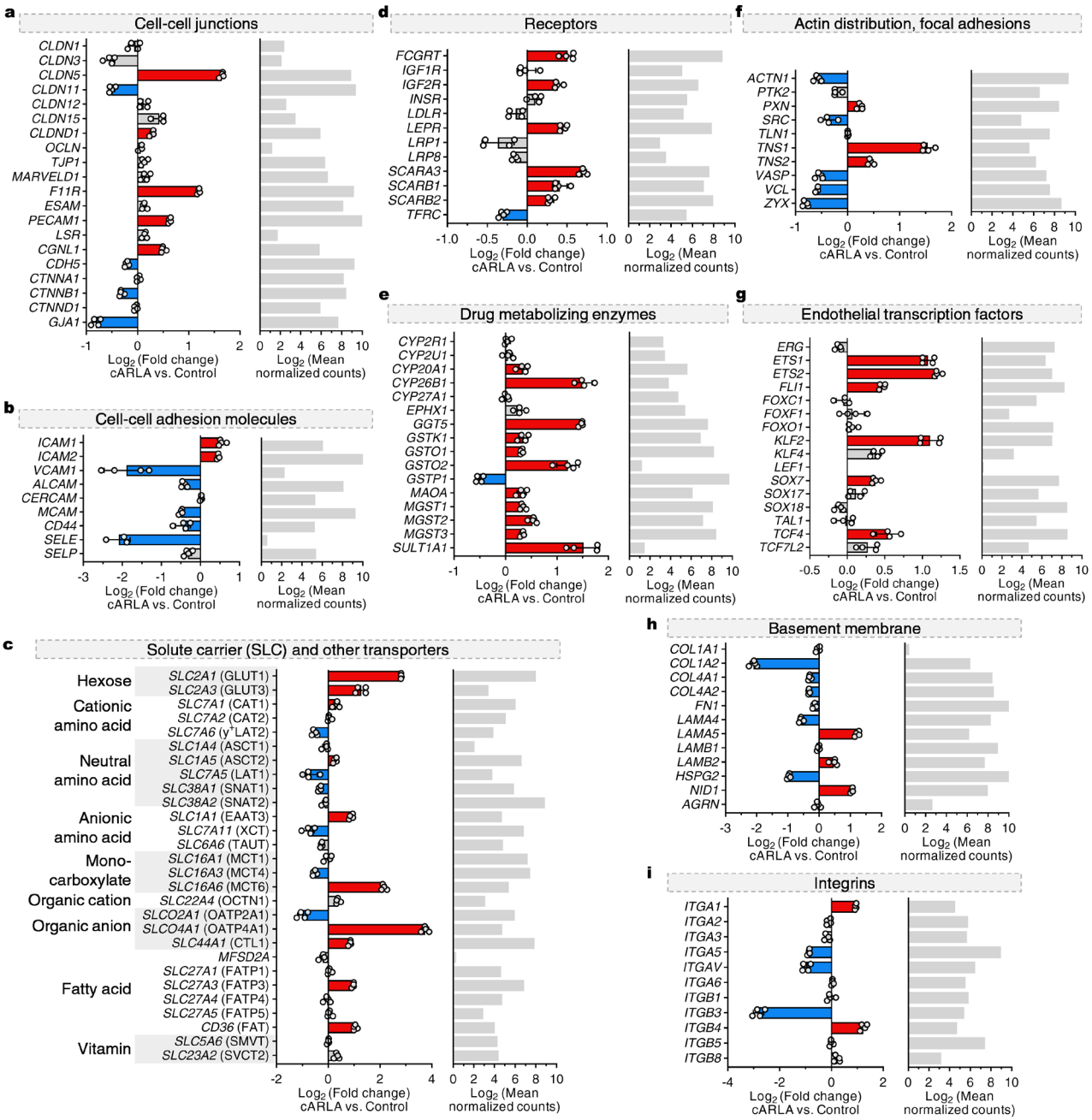

Extended Data Fig. 5. Changes in gene expression related to different aspects of BBB function in brain-like ECs. Gene expressional changes after 48 h cARLA treatment were determined using MACE-seq profiling and are presented in panels **a-i)** by category. Mean ± SD, *n*=4. Red and blue color indicates up- and downregulation, respectively, upon cARLA treatment.

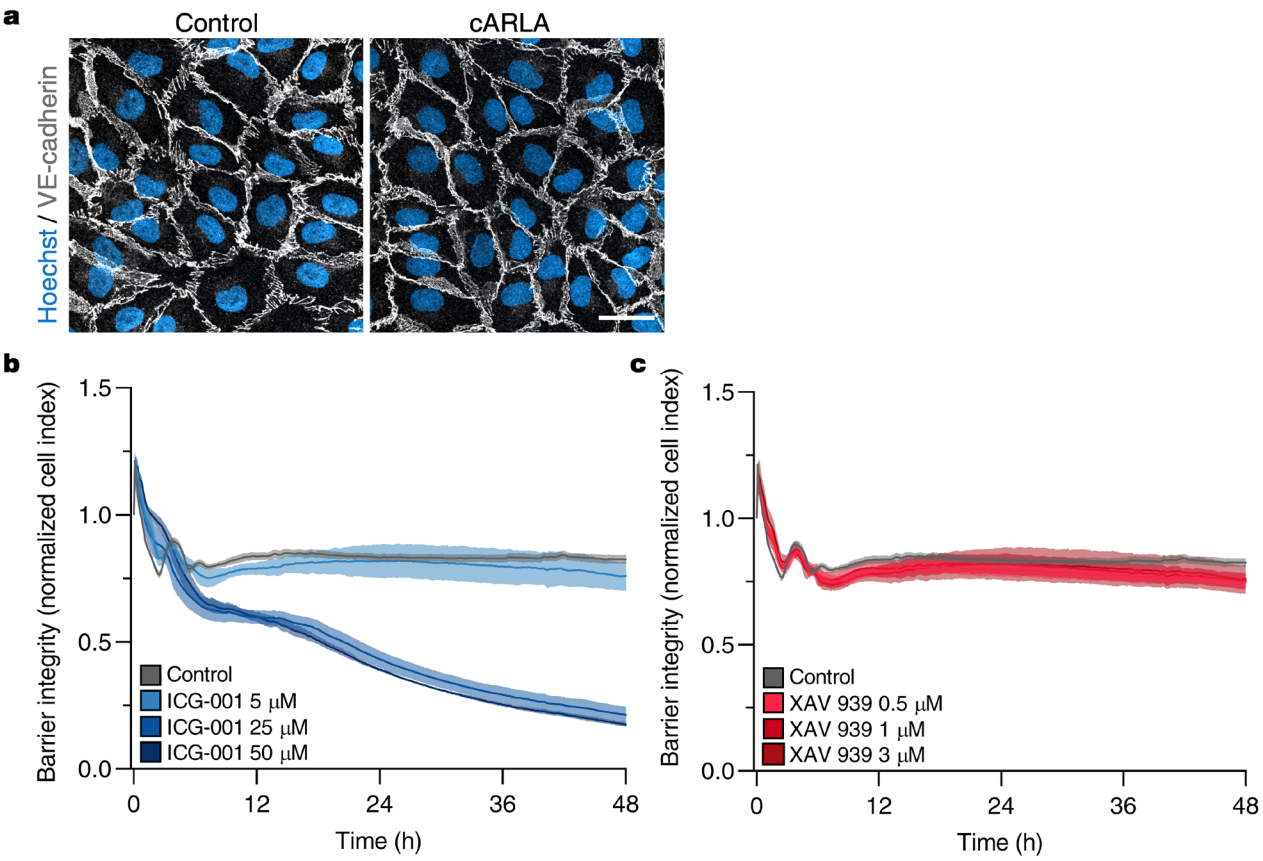

Extended Data Fig. 6. Additional experiments on Wnt/β-catenin signaling in brain-like ECs. **a)** Representative confocal microscopy images of VE-cadherin immunostaining (grey) show no disruption in VE-cadherin junctions upon 48 h cARLA treatment. Nuclei were stained with Hoechst (blue). Bar: 50 µm. **b)** Barrier integrity measured by impedance upon treatment with ICG-001, which specifically blocks the β-catenin-CBP interaction in the nucleus and **c)** XAV 939, which blocks the pathway upstream of nuclear translocation. Cells for this experiment did not receive cARLA treatment. Selected concentrations for further experiments were: ICG-001 5 µM, XAV 939 1 µM. Higher normalized cell index values and a higher area under the curve indicates increased barrier integrity. Mean ± SD, *n*=6.

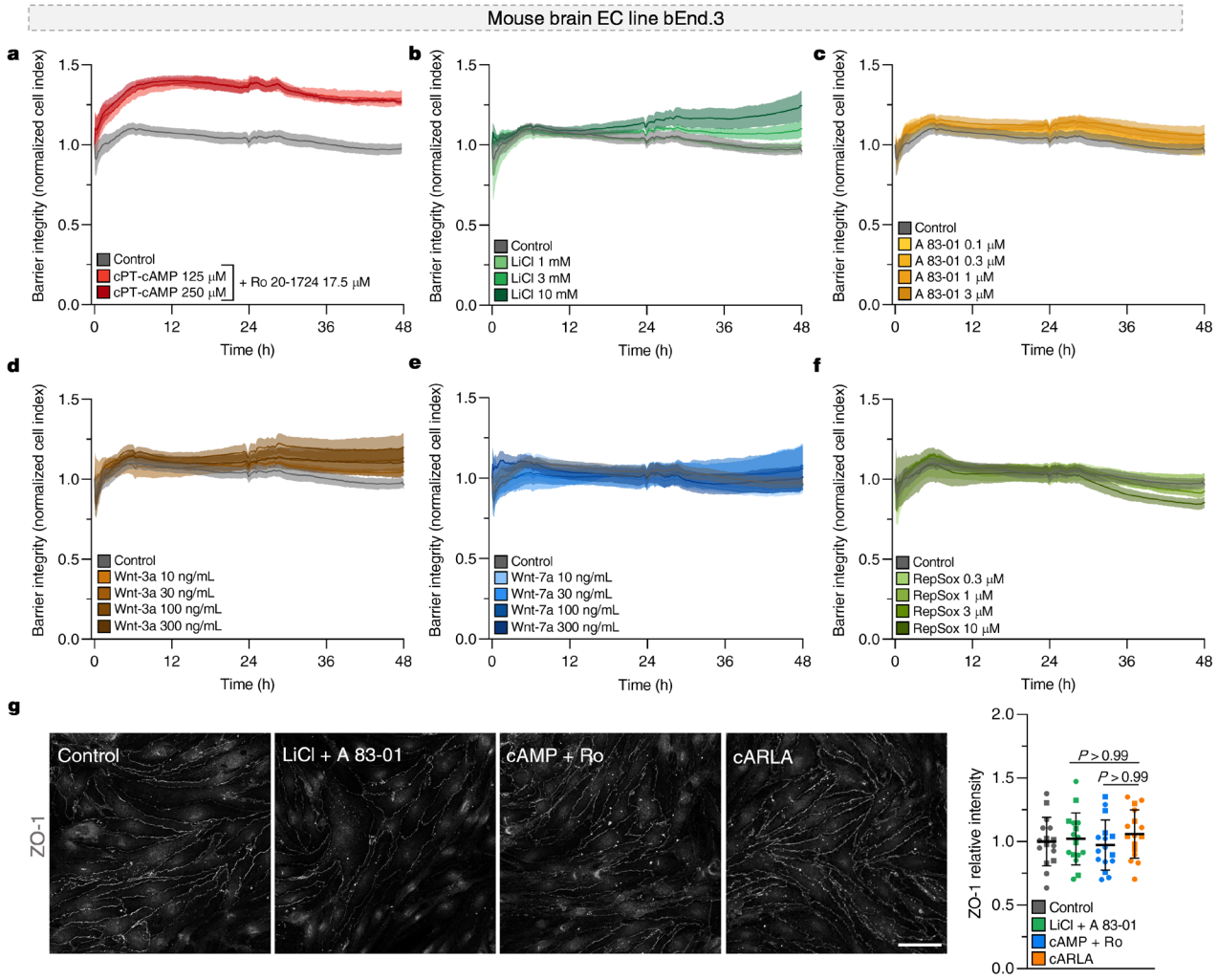

Extended Data Fig. 7. Different treatment concentrations are optimal for barrier integrity in mouse bEnd.3 cells. a-f) The effect of small molecules and recombinant proteins targeting single pathways on barrier integrity, measured by impedance. Selected concentrations for further experiments on bEnd.3 cells were: cPT-cAMP 125 µM, LiCl 10 mM, A83-01 1 µM, Wnt-3a 100 ng/mL, Wnt-7a 100 ng/mL, RepSox 1 µM. Higher normalized cell index values and a higher area under the curve indicates increased barrier integrity. Mean ± SD, *n*=5-6. **g)** Immunostaining of the tight junction protein ZO-1 in bEnd.3 cells after 48 h treatment. Bar: 50 µm. Quantification: Mean ± SD, ANOVA with Bonferroni's post-hoc test, *n*=16 from 2 independent experiments.

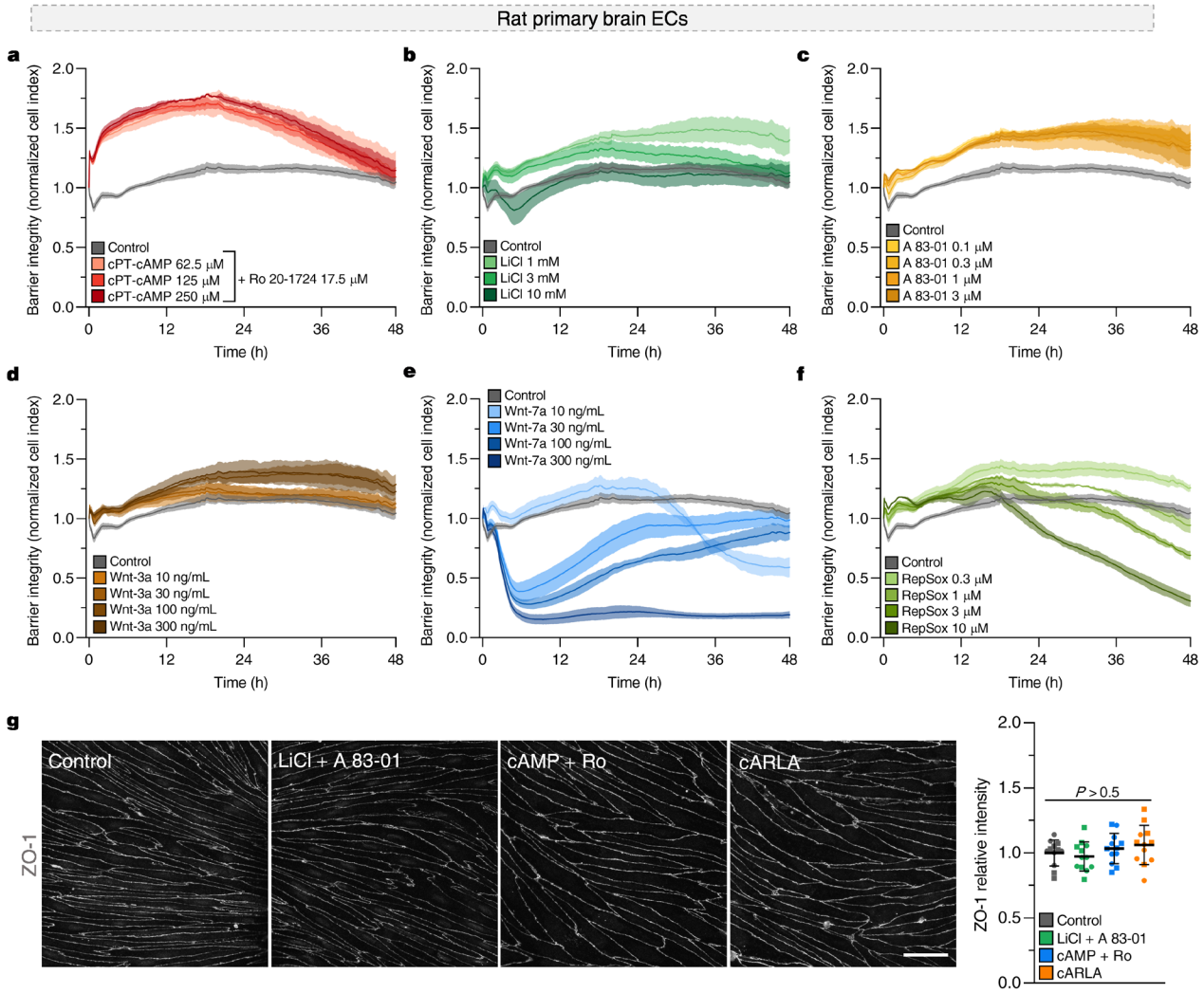

Extended Data Fig. 8. Different treatment concentrations are optimal for barrier integrity in rat primary brain ECs. a-f) The effect of small molecules and recombinant proteins targeting single pathways on barrier integrity, measured by impedance. Selected concentrations for further experiments on rat primary ECs and the EC-PC-AC co-culture were: cPT-cAMP 250 µM, LiCl 1 mM, A83-01 1 µM, Wnt-3a 100 ng/mL, RepSox 0.3 µM. Higher normalized cell index values and a higher area under the curve indicates increased barrier integrity. Mean ± SD, *n*=5-6. **g)** Immunostaining of the tight junction protein ZO-1 in rat primary brain ECs from EC-PC-AC co-cultures after 48 h treatment. Bar: 50 µm. Quantification: Mean ± SD, ANOVA with Bonferroni's post-hoc test, *n*=12 from 2 independent experiments.